RSC Advances




ROYAL SOCIETY OF CHEMISTRY

www.rsc.org/advances

# Oxidative esterification of furfural over Au-Pd/HAP-T and Au-Ag/HAP-T bimetallic catalysts supported on mesoporous hydroxyapatite nanorods.

Ramakrishnan Radhakrishnan, Kathiravan Kannan, Shathivel Kumarvel and Sivakumar Thiripuranthagan*

**ABSTRACT:** The conversion of furfural, a lignocellulose biomass, into fuels and value-added fine chemicals has attracted many researchers. In this study, structurally uniform and porous hydroxyapatite nanorods (HAP-T) with the gel composition of $1Ca^{2+}$: $0.66PO_4^{3-}$ : 0.3 CTAB: 120 $H_2O$ were synthesized under hydrothermal method. The synthesized HAP-T was impregnated with Au, Pd or Ag so as to obtain either monometallic (Au/HAP-T, Pd/HAP-T and Ag/HAP-T) or bimetallic ($Au_{1-x}Pd_x$/HAP-T and $Au_{1-x}Ag_x$/HAP-T) catalysts. The obtained hydroxyapatite catalysts were thoroughly characterized by using various analytical techniques such as FT-IR, XRD, BET, UV-DRS, XPS, HR-SEM & HR-TEM. A thorough characterization of the catalysts lead to the valid information that bimetallic $Au_{1-x}Pd_x$/HAP-T catalysts have core-shell bimetallic morphology, whereas the $Au_{1-x}Ag_x$/HAP-T catalysts have alloy morphology. The catalytic activities of the bare HAP-T, monometallic (Au/HAP-T, Pd/HAP-T and Ag/HAP-T) and bimetallic ($Au_{1-x}Pd_x$/HAP-T and $Au_{1-x}Ag_x$/HAP-T) catalysts were evaluated at atmospheric pressure towards the oxidative esterification of furfural to methyl 2-furoate using TBHP as oxidant and methanol as solvent. Among the various synthesized catalysts, $Au_{0.8}Pd_{0.2}$/HAP-T catalyst with core-shell structure showed the maximum conversion of furfural (94.2%) with very high selectivity towards methyl-2-furoate (99%). In addition, the efficiency of $Au_{0.8}Pd_{0.2}$/HAP-T catalyst was maintained even after 5 cycles, supporting the reusability and stability.

---

** Corresponding author*
*Catalysis Laboratory, Department of Applied Science and Technology, A.C.Tech Campus, Anna University, Chennai-25. E-mail: tssivakumar@yahoo.com; Tel.: 91-44-22359193.*

## 1. Introduction

Furfural is the dehydration product of naturally abundant C-5 sugars (arabinose & xylose) obtained from the biomass lignocellulose (hemicellulose fraction)[1,2]. Furfural, a natural precursor, is a bio based alternative platform molecule for the production of everything from medicines, pesticides, paints, plastics, commodity chemicals and solvents[3-5]. Currently furfural production is about 300 KT at a price of 2000$/ton and is being projected to increase[6]. It is a building block for several value added fine chemicals and fuels such as 2-methyl furan, furfuryl alcohol, furan, cyclopentanol, cyclopentanone, tetrahydrofurfuryl alcohol, 2-methyl tetrahydrofuran and $C_{10}$-$C_{15}$ coupling products. Hence it is identified as one of the most promising renewable chemicals for sustainable production of commodity chemicals and fuels. Hence valorization of furfural is the subject of interest to many researchers in the world. One of the authors had already reported the conversion of different biomasses into fuels[7-10]. The valorization process will be attractive only when (i) it is carried under mild conditions and (ii) it is environmentally benign. So it is very important to find a new pathway to convert furfural into commodity chemicals. Among the different valorization processes of furfural, the synthesis of esters particularly methyl 2-furoate find interesting applications in the fine chemical industries. These alkyl furoates are used in flavors and fragrance industries[11]. Furfural to methyl 2-furoate is typically an oxidation and esterification reaction. Conventionally methyl 2-furoate is prepared by oxidizing furfural with strong oxidizing agent such as $KMnO_4$ into furoic acid and then esterification using concentrated $H_2SO_4$ in methanol medium. The usage of such corrosive acid affects the environment badly. Hence it is desired to carry out this esterification reaction in one step that too under milder conditions but without using any corrosive reagents. Recent literature shows that it can be effected in mild conditions but by using bases such as NaOH, $CH_3ONa$,

etc.[12]. Since esterification of furfural using bases is also not a greener method, base free system is sought by the environmentally conscious scientists.

Hydroxyapatite [$Ca_{10}(PO_4)_6(OH)_2$], a calcium phosphate based biomaterial, apart from its biomedical and bioceramic application such as controlled drug and protein release, surface coatings for orthopaedic surgery and dental implants, it can be a best choice for catalyst support due to its ion-exchange capacity with various metal cations and anions, adsorption capacity, acid-base properties and thermal stability[13-18]. Not only that by tuning the Ca/P ratio one can tune the hydroxyapatite either for acid or base catalyzed reactions.

Various catalytic transformations were reported using hydroxyapatite as support for different transition metals[19-21]. $Ca^{2+}$ present in the hydroxyapatite lattice can also be exchanged with cations such as Cu, Ni, Zn, Fe and Co[22-26]. The partial exchange of $PO_4^{3-}$ with vanadate, tungstate and silicate are also possible[19, 27, 28]. Hence it is a versatile material for many catalytic applications. Studies on oxidative esterification of furfural over various Au supported catalyst have been reported earlier but they have certain disadvantages such as poor yield, usage of bases or requirement of severe reaction conditions such as high oxygen pressure[29-33]. The addition of second metal generally enhances the catalytic activity and stability due to the change in their electronic and geometric properties. In this context various bimetallic catalysts have been synthesized and their enhanced catalytic activities were reported. For example, Au/Pd bimetallic catalysts have shown excellent catalytic properties in ethanol oxidation under alkaline conditions vinyl acetate synthesis, benzyl alcohol oxidation and 1, 2-propanediol oxidation[34-37]. Similarly Au/Ag bimetallic catalysts were reported for the various catalytic transformations such as oxidation of benzyl alcohol, 1-phenyl ethanol, TMB, methanol to methyl formate, hydrogen from allyl alcohol, methyl acrylate, biomass to 2-HMF and 2,5-DMF, $N_2O$ decomposition, C-C coupling, but only few studies were reported on the oxidative esterification for furfural[38-46].

Hence it was envisaged to synthesize bimetallic catalysts supported over hydroxyapatites (HAP-T) and to explore the catalytic activities towards the oxidative esterification of furfural. Herein we report the synthesis of monometallic supported hydroxyapatites (Au/HAP-T, Ag/HAP-T & Pd/HAP-T) and bimetallic supported hydroxyapatites ($Au_1Pd_{1-x}$/HAP-T & $Au_{1-x}Ag_x$/HAP-T, X= 0.2, 0.4, 0.6, 0.8). Detailed characterization by various instrumental techniques and evaluation of catalytic activity towards the oxidative esterification of furfural are also reported here. We have studied the reaction with or without the addition of oxidant and with or without the addition of base. The results prove that the bimetallic catalysts are very active without the bases and very selective towards the desired product namely methyl 2-furoate. Hence it can be a good catalyst system for exploiting the renewable biomass into value added fine chemicals.

## 2. Experimental

### 2.1 Materials

Calcium nitrate ($Ca(NO_3)_2.4H_2O$, 99.9%), gold chloride trihydrate ($HAuCl_3.3H_2O$, 99.9%) and palladium acetate ($Pd(OCOCH_3)_2$, 99.98%) were obtained from Sigma Aldrich; Silver nitrate ($AgNO_3$, 99%), di-ammonium hydrogen orthophosphate ($(NH_4)_2HPO_4$, 99%) and cetyl trimethyl ammonium bromide ($C_{19}H_{42}BrN$, 99%) were purchased from SRL chemicals and sodium borohydride ($NaBH_4$, 98%) from Alfa Aesar was used in this study.

### 2.2 Synthesis of porous hydroxyapatite (HAP-T) nano rods

To the stoichiometric amount of calcium nitrate in 100 ml double distilled water, aqueous ammonia was added to maintain pH 10.5. Then aqueous di-ammonium hydrogen orthophosphate was added slowly to obtain a white gel. In another vessel, cetyl trimethyl ammonium bromide (CTAB) was dissolved in double distilled water and stirred for 1 hour. CTAB solution was slowly added to the above calcium phosphate gel with continuous stirring. The thickened gel was

then autoclaved at 453 K for 24 hrs. The upper transparent solution was decanted and the white mass was filtered through the Whattman filter paper, washed with 500 ml of double distilled water, dried at 383 K for 24 hrs, ground and finally calcined at 773 K, with the heating rate of 1°C/min. This procedure was adopted to get the gel composition of $1Ca^{2+}$: $0.66PO_4^{3-}$ : 0.3 CTAB: 120 $H_2O$. in which Ca/P was maintained at 1.67 for stoichiometric synthesis. The hydroxyapatite thus synthesized using the template is designated as HAP-T and without template was also synthesized and designated as HAP-D.

**2.2.1 Synthesis of monometallic Au/HAP-T, Ag/HAP-T and Pd/HAP-T catalysts.** To 1000 mg of hydroxyapatite synthesized using the above procedure, known volume of aqueous solution of $HAuCl_3.3H_2O$ (0. 05 mM) was added at the constant temperature of 353 K and stirred for 3 hrs so as to obtain 5 wt%. of Au over HAP-T. Then an aqueous solution of $NaBH_4$ (25 ml, 0.01M) was rapidly added to the above solution with vigorous stirring. Bluish-purple colour dispersion formed was allowed to stir for 1 hr, centrifuged, washed with de-ionized water and with ethanol twice. Finally the above synthesized material was dried at 343 K for 6 hrs, calcined at 623K under the air atmosphere for 2 hrs and completely reduced under the flow of hydrogen (0.2LMP) at 623K for 5 hrs to obtain the Au/HAP catalyst. Similar method was also adopted for the synthesis of Ag/HAP-T and Pd/HAP-T using $AgNO_3$ and $Pd(OAc)_2$ as precursors, so as to obtain 5wt.% of metal supported over HAP-T.

**2.2.2 Synthesis of bimetallic Au-Ag/HAP-T catalysts.** To 1000 mg of hydroxyapatite (HAP-T), known volume of aqueous solution of $HAuCl_3.3H_2O$ (0.05mM) and $AgNO_3$ were added simultaneously at the constant temperature of 353K and stirred for 6 hrs. Then an aqueous solution of $NaBH_4$ (25 ml, 0.01M) was rapidly added into the above solution with vigorous stirring. The colored dispersion was allowed to stir for 1 hr, centrifuged, washed with de-ionized water and ethanol twice. Finally the above synthesized material was dried at 343K for 6 hrs,

calcined at 623K under the air atmosphere for 2 hrs and completely reduced under the flow of hydrogen (0.2 LMP) at 623K for 5 hrs to obtain the Au-Ag/HAP catalyst. By varying Au and Ag contents, various catalysts such as $Au_{0.8}Ag_{0.2}$/HAP-T, $Au_{0.6}Ag_{0.4}$/HAP-T, $Au_{0.4}Ag_{0.6}$/HAP-T and $Au_{0.2}Ag_{0.8}$/HAP-T were prepared.

**2.2.2 Synthesis of bimetallic Au-Pd/HAP-T catalysts.** To 1000 mg of hydroxyapatite, known volume of aqueous solution of $HAuCl_3.3H_2O$ (0.05mM) and $Pd(OAc)_2$ were added at the constant temperature of 353 K and stirred for 6 hrs. Then an aqueous solution of $NaBH_4$ (20ml, 0.01M) was rapidly added into the above solution with vigorous stirring. The colored dispersion was allowed to stir for 1 hr, centrifuged, washed with de-ionized water and ethanol twice. Finally the above synthesized material was dried at 343K for 6 hrs, calcined at 623K under the air atmosphere for 2 hrs and completely reduced under the flow of hydrogen (0.2LMP) at 623K for 5 hrs to obtain the Au-Pd/HAP catalyst. By varying Au and Pd content, various catalysts such as $Au_{0.8}$ $Pd_{0.2}$/HAP-T, $Au_{0.6}$ $Pd_{0.4}$/HAP-T, $Au_{0.4}Pd_{0.6}$/HAP-T and $Au_{0.2}$ $Pd_{0.8}$/HAP-T were prepared.

**2.3 Characterization**

Powder X-ray diffraction data (P-XRD) were collected on a Rigaku ultima+ diffractometer using Cu-$K_\alpha$ ($\lambda$=1.54056A°) radiation with a solid-state detector at 40kV and 40mA. The data were recorded in the 2θ range from 1-8° (narrow range) and 2θ range from 10-80° (wide range) with 2θ step size of 0.01° and step time of 10 s. The obtained data were analyzed using Origin 8 software for the determination of phase composition and crystallinity. The peaks were indexed on a hexagonal unit using $R_3C$ space group. The standard JCPDF card no.09-432 was used for comparing the hydroxyapatites. Fourier Infra Red spectra (FT-IR) were recorded on a Thermo-Nicolet IR 2000 spectrophotometer in wavenumber range of 4000–400 $cm^{-1}$. Nitrogen adsorption and desorption isotherms studies were performed at 77 K on a BELSORP mini, BEL Japan instrument. Prior to analysis, the samples were degassed at 473 K for 2 h under nitrogen

atmosphere. The UV–Visible spectra of the solid samples were recorded directly using a JASCO V-650 UV-Vis spectrophotometer equipped with an integrated sphere for diffuse reflectance studies. X-ray photoelectron spectroscopy (XPS) measurements were performed to find out the elements present in the catalyst on an ESCA+, Omicron Nanotechnology ESCA Probe spectrometer with monochromatized $AlK_{\alpha}$ X-rays (energy: 1486.6 eV) 300W with base pressure of $5x10^{-5}$ mB. Sputter-cleaned Cu $_{2p3/2}$ (932.7 eV) and Au $_{4f7/2}$ (84.0 eV) core level peaks (from foils) were used to calibrate the XPS instrument. The catalyst samples were pelletized, dried under vacuum and mounted in the sample port. Spectra in the required binding energy range were collected for 8 times (except survey scan) and an average spectrum was taken. The binding energy (B.E) scale was referenced by setting the C (1s) binding energy (B.E) of adventitious carbon to 284.6 eV. XPS high-resolution scans were performed for the $Au4f_{5/2}$, $Au4f_{7/2}$, $Pd3d_{3/2}$, $Pd3d_{5/2}$, C1s, $Ca2p_{3/2}$, $Ca2p_{1/2}$, P2p, and O1s core levels. Quantitative determination of different elements present in the hydroxyapatite was carried out by Inductive coupled plasma (ICP) technique using Perkin Elmer Optima 5300 DV. 200 mg of samples were digested in Con. nitric acid and diluted prior to the analysis. Particle morphology and structure of the hydroxyapatites were studied by using Quanta 200 FEG scanning electron microscope (HR-SEM). Powdered samples were air dispersed over the carbon tape and conductivity was enhanced by gold sputtering. The High resolution transmission electron micrographs (HR-TEM) were recorded using JEOL JEM-2100JF working at the operating voltage of 200KeV. Powder samples were dispersed in ethanol, ultrasonicated for 10 minutes prior to analysis placed over holey carbon coated Cu grid, dried at ambient conditions and mounted for analysis.

**2.4 Catalytic studies**

The liquid phase oxidative esterification of furfural in the presence of methanol as solvent and using tert-Butyl hydroperoxide (TBHP) as an oxidant was investigated at 393K. 300µl of

furfural, 3 eq. of TBHP (70%) and 50 mg of catalyst (Au - 20 mol%) were added to 20ml of methanol and the reaction was carried out in liquid phase. The progress of the reaction was monitored by thin layer chromatography (TLC) using of petroleum ether: ethyl acetate (9:1) as mobile phase. After the reaction, catalyst was separated by centrifuging and then treated with chloroform water mixture in a separating funnel for the removal of excess of methanol. The golden yellow layer was separated and dried over anhydrous sodium sulphate. Sample aliquots (30μL) was filtered through the nylon syringe filters (0.22 microns) and analyzed using a Shimadzu GC-17A gas chromatograph equipped with a capillary column and a flame ionizing detector (FID).

## 3. Results and discussion

### 3.1 FT-IR spectral analysis

Figure.ESI.1 shows the FT-IR spectra of HAP-T synthesized via hydrothermal method using CTABr mediated template and is compared with the HAP synthesized via direct precipitation method (HAP-D) and gold loaded (Au/HAP-T) apatite catalysts. The sharp and small peak around 3570 $cm^{-1}$ is due to the stretching mode of non hydrogen bonded OH groups of the hydroxyapatites. The broad band around 3431 $cm^{-1}$ and 1647 $cm^{-1}$ are due to stretching mode of hydrogen bonded OH group and ν2 bending mode present in the adsorbed water molecules. The 1093 $cm^{-1}$ and 1035 $cm^{-1}$ band arise from triply degenerate $\nu_3$ antisymmetric PO stretching mode of $PO_4^{3-}$ , 963 $cm^{-1}$ peak is due to the nondegenerate PO symmetric stretching mode $\nu_1$ $PO_4^{3-}$, 604 $cm^{-1}$ and 568 $cm^{-1}$ band arising from components of the triply degenerate $\nu_4$ OPO bending mode of $PO_4^{3-}$ and 473 $cm^{-1}$ is due to the doubly degenerate $\nu_2$ OPO bending mode of $PO_4^{3-}$. The FT-IR spectra of all the hydroxyapatites look alike, indicating the structural similarity in all of them and are in good agreement with the reports[47,48]. The incorporation of Au followed by reduction in the Au/HAP-T also did not affect the structural features of hydroxyapatites.

### 3.2 Powder x-ray diffraction

The small and wide angle x-ray powder diffraction patterns of bare hydroxyapatite (HAP-T) are shown in Fig. 1 & 2

**Figure.1 & Figure.2**

The broad peak appearing from 2θ = 2° to 4° indicates the mesoporous nature of synthesized hydroxyapatite. However the broadness of the peak suggests that they have irregular mesopores. The high angle XRD shows intense and well resolved peaks confirming the nature of crystalline hydroxyapatite. The x-ray diffraction patterns were identified and indexed in comparison with the standard JCPDS-ICDD values[49]. The standards with card nos. 04-932 ($Ca_{10}(PO_4)_6(OH)_2$), 09-0169 (β-$Ca_3(PO_4)_9$), 04-0777(CaO) and 04-0733($Ca(OH)_2$) were used to check whether these compounds were present in the hydroxyapatites. On comparison, it was found that none of the above was found and this indicates the phase purity of hydroxyapatites. The average crystallite size ($X_S$, nm) in a direction perpendicular to the crystallographic plane based on Scherrer formula was calculated by using the equation:

$$X_s = \frac{0.9 \times \lambda}{(\beta_{hkl} \times \cos\theta)}$$

Where, λ – is the wavelength of the monochromatic x-ray beam (Cu-$K_{\alpha 1}$, 1.54056A°); $\beta_{hkl}$ – broadening of the hkl diffraction peak measured at half of its maximum intensity (radians) and θ – diffraction angle[50].

The unit cell lattice parameters were indexed using a hexagonal unit cell lattice and determined using the following formula and were found to be a = b = 9.432A°, c = 6.881A°.

$$\frac{1}{d^2} = \frac{4}{3}\frac{[h^2 + hk + k^2]}{a^2} + \frac{l^2}{c^2}$$

These values are found to be in good agreement with our reported literature[51]. Using the obtained lattice parameters values of a and c, the volume of the unit cell was calculated and was found to be 530.14 $cm^3$:

$$V = a^2c \times \sin 60^\circ$$

Figure.3 shows the wide angle x-ray powder diffraction patterns of Au/HAP-T, Pd/HAP-T and $Au_{1-x}Pd_x$/HAP-T catalysts(x=0.2-0.8)

**Figure.3**

The appearance of diffraction peaks at 2θ= 39.68(111), 46.48(200), 68.64(220) confirm the presence of Pd and at 2θ=38.24(111), 44.32(200), 64.4(220) confirm the presence of Au. The peaks are indexed in the FCC lattice and compared with the standard JCPDS cards 41-1043(Pd) and 65-2870(Au) respectively. Using the Scherrer equation the average particle size was calculated and they were found to be 10.9 nm for Au/HAP-T, 9.7 nm for $Au_{0.8}Pd_{0.2}$/HAP-T, 9.3 nm for $Au_{0.6}Pd_{0.4}$/HAP-T, 9.5 nm for $Au_{0.4}Pd_{0.6}$/HAP-T, 9.8 nm for $Au_{0.2}Pd_{0.8}$/HAP-T and 13.7 nm for Pd/HAP-T. It was observed that the bimetallic shows smaller particles than the monometallic hydroxyapatites as reported[52,53]. The average particle sizes of metal particles calculated from the XRD are given in Table.1.

**Table -1**

A well separable peak for the metal species indicates that the nano metallic particles in either mono or bimetallic are well dispersed over the porous hydroxyapatite. The peak intensity of Au in the hydroxyapatites of $Au_xPd_{x-1}$/HAP-T (x=0.4, 0.6 & 0.8) was found to be almost the same, whereas the peak intensity of Pd increases with concentration. Such possibility will occur only when there is a core-shell formation with Au in the core and Pd as the shell. Such formation of core –shell is justified from the changes in the interplanar spacing and lattice parameter. As

per the Vegard's law, the formation of ordered bimetallic species can be confirmed from the linearity of the plot of molar ratio Vs d-spacing (Figure.ESI2). The corresponding d-spacing and lattice parameter of both mono and bimetallics of Au and Pd are given in Table 2. Since inter-planar spacing "d" is proportional to lattice parameter "a", any effect would change the interatomic distance which in turn changes the geometric and electronic properties also.

**Table.2**

The linearity reveals that both the metals are in zero oxidation state, the existence of oxides of Au and Pd are ruled out. The absence of peaks at 2θ = 33.216(002), 34.352(101) and 42.854(110) indicates the absence of PdO species(JCDFS card no. 88-2434) and this further confirms that both the Au and Pd were completely involved in the formation of bimetallics. The fact that (002) plane corresponding to c-axis of the hydroxyapatite remains unaffected confirms that both the crystallinity and stability are retained even after the impregnation of metals and reduction under $H_2$ atmosphere.

Figure.4 shows the wide angle x-ray powder diffraction patterns of Au/HAP-T, Ag/HAP-T and $Au_{1-x}Ag_x$/HAP-T catalysts(x=0.2-0.8).

**Figure.4**

On comparison of these powder diffraction patterns with standard JCPDS of Au(04-0784) and Ag(04-0783), it was found that the peaks match at 2θ= 38.04°(111), 44.2°(200) and 64.72°(220) and are indexed in the face centered cubic (*fcc)* lattice. The powder diffraction patterns further confirm the absence of peaks of the oxides of Au and Ag in the synthesized hydroxyapatites. Since the d values of Au ($d_{111}$=0.2355nm) and Ag ($d_{111}$=0.2359nm) are close to each other, the powder diffraction patterns of both mono and bimetallics of Au and Ag

hydroxyapatites look alike. The closeness of the interplanar spacing "d" and the lattice parameter "a" make it difficult to distinguish the peaks not only for the (111) plane but also with the other planes such as (200) and (220). The powder diffraction patterns of mono and bimetallics shows sharp peaks indicating high crystallinity. The particle size of Au/HAP-T (10.9 nm) is the least in the series whereas it is the highest for the Ag/HAP-T (32.7 nm). The increase in Ag content in bimetallic hydroxyapatites increases the particle size[54,55]. The average particle sizes calculated from the XRD are given in Table.1.

### 3.3 UV-Visible diffuse reflectance studies (UV-DRS)

Figure.5 shows the UV-Visible diffuse reflectance spectra of monometallic (Au/HAP-T & Pd/HAP-T) and bimetallic ($Au_{1-x}Pd_x$/HAP-T) hydroxyapatites. Among the hydroxyapatites, the monometallic Au/HAP-T shows surface plasmonic resonance(SPR) band around 520 nm due to the transition of $e^-$ from occupied 5d to vacant 6sp, which corresponds to the band gap of 2.4 eV[56,57]. Such SPR transition is not seen in Pd/HAP-T. With increase in the Pd concentration in the bimetallics, the intensity of the surface plasmonic resonance band decreases. The dramatic decrease in the intensity of this band occurred even when a small amount of Pd (x = 0.2) was incorporated. The interaction between Au and Pd in the bimetallic allows a large change in the electronic properties as reported[58,59]. The absence of SPR bands at 308 nm and 407 nm indicates the absence of other ionic species such as $Au^{3+}$ and $Pd^{2+}$ respectively[60]. In any bimetallic formation, either a core-shell structure or alloy structure is possible. The fact that the intensity of the surface plasmonic resonance (SPR) decreases with the increase in the concentration of Pd suggest the formation of core-shell structure of Au/Pd-HAP-T. When a small amount of Pd is present in bimetallics, it forms a thin non-homogeneous shell over Au core. When the Pd concentration increases, the bimetallic hydroxyapatites show decrease in the intensity of SPR band around 520 nm and get completely vanished beyond Pd = 0.4. This is mainly due to the

thick coverage of Pd over Au. Such reduction of SPR bands when any of the group 10 metals is added to Au was also reported earlier[60,61]. Such large change in the electronic properties was also reported[62].Yong D et. al. reported the reorientation of the Au-Pd as core-shell structures when the bimetallics was heated to 523K leading to the formation of alloy[63]. However the bimetallic hydroxyapatites synthesized by us did not reorient and was intact even after the reduction at 623K for 5hrs.

**Figure.5**

Figure.6 shows the UV-Visible diffuse reflectance spectra of monometallic (Au/HAP-T & Ag/HAP-T) and bimetallic ($Au_{1-x}Ag_x$/HAP-T) hydroxyapatites.

**Figure.6**

The UV-DRS spectra of Au/HAP-T and Ag/HAP-T are different from that of the Au-Pd/HAP-T system. In the UV-DRS spectra of Au and Ag system, the SPR bands occur at two different wavelengths at 526nm and 470nm for the Au/HAP-T and Ag/HAP-T respectively[64]. In this bimetallic, the increase in Ag wt. % has direct impact on the shifting of the surface plasmon resonance (SPR) bands; 511.6nm for $Au_{0.8}Ag_{0.2}$/p-HAP, 500.2nm for $Au_{0.6}Ag_{0.4}$/p-HAP, 489.5nm for $Au_{0.4}Ag_{0.6}$/p-HAP and 476.2nm for $Au_{0.2}Ag_{0.8}$/p-HAP[65]. The formation of alloy structure[66-68] or core-shell structure[69-71] can be derived by the shift in the SPR bands. The absence of two separate SPR bands indicate that the bimetallic is not a physical mixture of Au-Ag system and also rules out the $Au_{core}/Ag_{shell}$ or $Ag_{core}/Au_{shell}$ structure[72-74]. The formation of single SPR band and its gradual blue shifting and broadening with increase in Ag content in the bimetallic suggest the complete interaction between Au and Ag forming an alloy at all the concentrations (Figure.ESI3). The linearity in the plot between % mole fractions of Ag to $\lambda_{max}$

of SPR bands further confirms the formation of alloy structure (Figure.ESI4) for Au-Ag bimetallic.

### 3.4 BET Nitrogen Adsorption-Desorption Measurements

To check whether the synthesized hydroxyapatite is mesoporous in nature, nitrogen adsorption and desorption isotherms were constructed at liquid $N_2$ temperature in the relative partial pressure of $P/P_0$=0.05 to 1.0. Figure.7 shows the BET adsorption isotherm and (b) pore size distribution of HAP-T. This figure shows that the hydroxyapatite exhibits a type IV isotherm with steep H1 hysteresis loop occurring in the partial pressure between 0.6 and 0.9 confirming the presence of mesopores with open ends in the hydroxyapatites. The BET surface area and the pore volume of the hydroxyapatite were also calculated and they were found to be 44 $m^2$/gm and 0.2485 $cm^3$/gm. The BJH pore size distribution of the HAP-T sample is shown in Figure.8.

**Figure.7 & 8**

The synthesized hydroxyapatite has large population of the pores with diameter of 2.4 nm, 3.1 nm and 5.4 nm. The HR-TEM micrograph (discussed later) also confirms pores in the above mentioned ranges. Hydroxyapatites with such different pore diameters have also been reported[75-77].

### 3.5 X-ray photoelectron spectra

X-ray photoelectron spectra (XPS) were recorded for Au-Pd-HAP and Au/Ag- HAP catalysts to understand their structural and electronic properties.

**Figure.9**

Figure.9 illustrates the XPS survey spectra of $Au_1$-HAP. The measured XPS core levels of Ca($Ca_{2p3/2}$-346.6 eV, $Ca_{2p1/2}$-350.1eV), P ($P_{2p}$- 132.6eV) and O (O 1s) were in good agreement

with the reported literature[78,79]. The Ca/P ratio calculated from XPS lie in the range of 1.55-1.59 which is almost close to both the Ca/P=1.63 obtained from the ICP and theoretical Ca/P= 1.67. The determined Ca/P ratio rules out the formation of other calcium phosphate species such as α-TCP, β-TCP, ACP(Ca/P=1.50), OCP(Ca/P=1.3) and DCPD(Ca/P=1.0). Hence XPS study further confirms the phase formation and stability of HAP-T besides FT-IR and XRD studies[79, 80].

Figure.10 shows the XPS spectra of the Au, Ag and Pd core levels of Au/HAP-T, Ag/HAP-T and Pd/HAP-T. The binding energy of Au ($Au_{4f7/2}$ – 83.37eV & $Au_{4f5/2}$ – 87.03eV), Ag ($Ag_{3d5/2}$ – 367.4 eV & $Ag_{3d3/2}$ – 373.3eV) and Pd ($Pd_{3d3/2}$ – 334.9 eV & $Pd_{3d5/2}$ – 340.3eV) are in agreement with the literature values[81].

**Figure.10**

The XPS spectra of $Au_1Pd_{1-x}$/HAP-T catalysts are shown in Figure.11. From the Fig. the binding energies and surface concentration of Au and Pd were calculated and given in Table.3.

**Figure.11**

**Table.3**

The Table.3 also contains the theoretical and ICP values of metals content and their surface concentration. The bimetallics are present in the surface in significant quantities. In the core-shell arrangement, there are possibilities for the formations of either $Au_{core}$-$Pd_{shell}$ or $Pd_{core}$-$Au_{shell}$. Due to the higher reduction potential, electronegativity and electron affinity of $Au^{3+}$, Au gets reduced first forming core when compared to Pd. In this Au-Pd system, Au gains sp $e^-$ from Pd, whereas Pd gains d $e^-$ from Au and hence the stabilization of Au-Pd core-shell arrangement is mainly due to the net charge transfer[82]. The gain of d-character coupled with better dispersion of Pd over Au, makes it a better catalytic system[83]. The intensity of the Au peaks at 83.37eV and 87.03eV decrease with increase in the concentration Pd and vanish completely, while the Pd peaks at 334.9eV and 340.3eV increases with increasing Pd content.

The complete disappearance of the peaks could be explained only when the formation of bimetallic takes place through core-shell arrangement. At higher concentration of Pd in bimetallics, the envelope of Pd layer over gold takes place. This increase in the thickness of Pd over Au suppresses the existence of peaks for Au. This study again confirms the $Au_{core}$-$Pd_{shell}$ bimetallics. Similar synthesis of core-shell structures of Au-Pd bimetallics have been reported [84-86]. Figure.12 illustrates the XPS spectra containing the core levels of Au 4f, Ag 3d of $Au_1Ag_{1-x}$/HAP-T catalysts. The alloy formation between Au-Ag is further supported by the XPS analysis. The surface concentration of Au and Ag over the hydroxyapatite (HAP-T) was calculated from the intensity of the peak obtained at respective binding energies and the values are given in Table.4.

**Figure.12**

**Table.4**

A reasonable amount of Au and Ag is present on the surface of the hydroxyapatite. On increasing the concentration of Ag from 0.2 to 1, i.e. from $Au_{0.8}Ag_{0.2}$/HAP to $Ag_1$/HAP the intensity of the Au peaks at $Au_{4f7/2}$-83.57eV and $Au_{4f5/2}$-87.22eV decreased and the intensity of the Ag peak at $Ag_{3d5/2}$-367.2 eV and $Ag_{3d1/2}$-372.9 eV increased. In the Au/Pd system, the intensity of the Au core peaks vanished, but in Au/Ag system, even at $Au_{0.2}Ag_{0.8}$/HAP, the Au core peaks are not vanished. The presence of peaks even at high loading of Ag suggests the formation of alloy structure rather than core-shell system. Previous reports also support the Au/Ag alloy structure formation[87].

**3.6 Electron microscope studies of hydroxyapatite**

The surface topography and morphology of the HAP-T synthesized are depicted in HR-SEM and HR-TEM images (Figure.13).

**Figure.13**

The nano rods ≈ 250nm x 40nm (length x breadth) are seen in the HR-SEM micrographs (Figure.13a). All the nano rods were found to have similar size. The HR-TEM micrographs of these nano rods (Figure.13b & 13c) confirm the hexagonal shape with the size of 207nm x 38nm. The pores ≈ 6nm were also clearly seen on the hydroxyapatites nano rods (Figure.13d). Further magnification shows the lattice fringes with $d_{002}$=0.347nm and indicates the preferential growth along the c-axis (Figure.13e). This is in agreement with the XRD pattern. Hydroxyapatites with similar d-spacing were also reported in the literatures[88]. The SAED patterns (Figure.13f) corresponding to the strong reflections at $d_{002}$ = 0.346nm, $d_{211}$ = 0.282nm, $d_{210}$ = 0.312nm, $d_{112}$ = 0.278nm and $d_{213}$ = 0.185nm reveal the polycrystalline nature of the hydroxyapatites. This HR-TEM result coincides with the powder diffraction results discussed earlier.

The HR-TEM images of the monometallic Au/HAP-T, Pd/HAP-T and Ag/HAP-T are shown in Figures.14 (a-c). In all the micrographs the presence of corresponding metal particles was seen. Among the metal nano particles, Au particles are the smallest, and Ag particles are the biggest. The lattice fringes of the 002 plane corresponding to monometallic hydroxyapatites are shown in Figure 14(d-f). The d-values are also in clear agreement with the values obtained from the powder diffraction patterns.

**Figure.14**

The presence of lattice plane at $d_{111}$(0.235nm) and $d_{200}$(0.203nm) confirms the presence of Au, the lattice planes at $d_{111}$(0.225nm) confirms the presence of monometallic Pd and the lattice planes at $d_{111}$(0.237nm) confirms the presence of Ag as shown in Figure14(d-f). The HR-TEM images of the most active bimetallic hydroxyapatite of $Au_{0.8}Pd_{0.2}$/HAP-T with different magnifications are shown in Figure.15(a-c).

**Figure.15**

The HR-TEM micrographs reveal the porous nature of the hydroxyapatite (white dots) and metal particles (black dots). The uniform distribution of the bimetallics over HAP-T was clearly seen in the Figure 15d. The existence of bimetallic particles in $Au_{0.8}Pd_{0.2}$/HAP-T can be easily understood from their corresponding d values as shown in Figures.15e. As the concentration of the Pd in $Au_{0.8}Pd_{0.2}$/HAP-T is low a thorough coverage of Pd is not seen ($d_{111}$=0.225nm for Pd & $d_{111}$=0.235nm for Au), whereas in the other bimetallic of $Au_{0.6}Pd_{0.4}$/HAP-T a better coverage of Pd over Au is seen Figure.15f. The higher coverage of Pd over Au is due to the higher concentration of Pd in the bimetallic. Hence HR-TEM studies further confirm the formation of Au-Pd core-shell besides UV-DRS, XRD and XPS observations.

### 3.7 Catalytic studies of mono and bimetallic hydroxyapatites

Catalytic oxidation esterification of furfural was carried out in a batch reactor using methanol as solvent, TBHP as an oxidant over mono and bimetallic catalysts. Two different products namely methyl 2-furoate and 2-furaldehyde-dimethyl acetal were formed . No alkyl peroxides were formed.

**3.7.1 Effect of Reaction Temperature.** The effect of reaction temperature on the conversion of furfural and the selectivity towards methyl 2-furoate was first studied in the temperature range of 333K to 413K over Au/HAP-T and the results are given in Table.5

**Table.5**

The Au/HAP-T catalyst showed the highest conversion at 413K and highest selectivity towards methyl 2-furoate at 393K. Since large amount of the undesired products namely 2-

furaldehyde-dimethyl acetal is formed at 413K, temperature of 393K was optimized for further studies. Table.6 contains the results obtained in the oxidative esterification of furfural over the $Au_1Pd_{1-x}$/HAP-T bimetallic catalysts at the optimized reaction temperature of 393K. Between the two monometallic Au/HAP-T and Pd-HAP-T catalysts, the latter shows higher conversion of furfural (86.6%) than Au/HAP-T (76%). Among the bimetallic hydroxyapatites, $Au_{0.8}Pd_{0.2}$/HAP-T showed the highest conversion of 94.2% of furfural and the highest selectivity (99%) towards methyl 2-furoate. As far as selectivity towards methyl 2-furoate is concerned, a contrast behavior is shown by the monometallic hydroxyapatites, i.e Au/HAP-T showed higher selectivity of (94.2%) than Pd/HAP-T (2.3%).

**Table.6**

The results suggest that the introduction of Pd into Au/HAP-T increases the conversion, but decreases the selectivity towards methyl 2-furoate. However a significant increase in both conversion and selectivity was seen when small amount of Pd was introduced in to Au/HAP-T. The $Au_{0.8}Pd_{0.2}$/HAP-T catalyst shows the highest conversion of 94.2% and almost 99.0% selectivity towards the desired product of methyl 2-furoate. Hence this study reveals the significance of the interaction of low levels of Pd in $Au_{0.8}Pd_{0.2}$/HAP-T. As far as the bimetallics are concerned, the formation of the other products namely 4-furaldehyde-dimethylacetal was also found to increase with increase in the Pd content. Pd/HAP-T although show significant conversion, the selectivity towards methyl 2-furoate was too low (2.3%). In the Pd-rich bimetallic, a core-shell arrangement is completely formed. The Au clusters are not exposed to reactant molecules and hence results in poor conversion and selectivity. Similarly among the Au-Ag bimetallics (Table.7), $Au_{0.8}Ag_{0.2}$/HAP-T was found to convert 89.6% of furfural with

selectivity as high as 99% towards methyl 2-furoate, whereas the Ag/HAP-T showed poor selectivity (25%) to methyl 2-furoate.

**Table.7**

**3.7.2 Effect of addition of base in the oxidative esterification of furfural.** In the present study TBHP has been used for the oxidative esterification of furfural. In order to check the effect of other oxidants in the formation of ester, air or oxygen was bubbled into the reactor and the products were analyzed by gas chromatograph. The conversion and selectivity towards the two different products namely methyl 2-furoate and 4-furaldehyde-dimethyl-acetal are given in Table.8.

**Table.8**

It was found that the most active catalyst namely $Au_{0.8}Pd_{0.2}$/HAP-T did not convert furfural in air medium and only converted 5.8% in $O_2$ atmosphere. In general oxidative esterification reactions are carried out in the presence of base such as NaOH, $NaOCH_3$, $K_2CO_3$ . Hence in order to check the influence of the base on the conversion and selectivity, 5ml of 10% Aq. solution of NaOH/$NaOCH_3$/$K_2CO_3$ was added and the reactions were performed in $O_2$ atmosphere under the optimized conditions and the results are given in Table.8. It was found that the addition of base has tremendous improvement on the conversion and selectivity. Among the bases, $NaOCH_3$ was found to have the maximum conversion of furfural (78.1%) with the highest selectivity of (96%) towards methyl-2-furoate. Since the bases are corrosive in nature, another oxidant namely TBHP has been used and the reactions were carried out with and without oxygen. Replacement of base with TBHP yielded remarkable results both in conversion and selectivity. The usage of $O_2$ in addition to TBHP in the reaction over the most active catalyst has

no effect on the conversion and selectivity. This study clearly indicates that such oxidative esterification can be successfully carried out in base free and environmentally benign conditions.

**3.7.3 Effect of recyclability of $Au_{0.8}Pd_{0.2}$/n-HAP on the oxidative esterification of furfural**. The best catalyst namely $Au_{0.8}Pd_{0.2}$/HAP-T was recycled for 4 more times to check efficiency of the catalyst to convert furfural into methyl 2-furoate and the results are shown in Figure.16. It clearly shows that there is only ≈ 4% difference in the conversion at the end of the $5^{th}$ cycle. However there is no difference in the selectivity towards methyl 2-furoate. It remained around 99%. This study confirms the stability of the $Au_{0.8}Pd_{0.2}$/HAP-T catalyst.

**Figure.16**

## 4. Conclusion

In summary, we succeed in the hydrothermal synthesis of mesoporous hydroxyapatite nanorods (HAP-T) using CTAB as template. Mono and bimetallics of Au, Ag and Pd were impregnated and reduced simultaneously over hydroxyapatite nanorods (HAP-T) with better dispersion of the metal nanoparticles. Among the bimetallics, Au-Pd adopted core - shell morphology while the Au-Ag system showed alloy morphology over hydroxyapatite nanorods. The FT-IR, XRD and XPS analyses supports the formation and stability of the hydroxyapatites. $Au_{core}$-$Pd_{shell}$ and $Au_{alloy}$-$Ag_{alloy}$ morphology over HAP-T were confirmed by UV-DRS, HR-TEM and XPS analyses. Mesoporosity of the synthesized HAP-T was confirmed by BET measurements. The optimized reaction temperature for the oxidative esterification of furfural was found to be 393K. Introduction of small amounts of either Pd or Ag in Au-HAP-T increased the conversion of furfural. Among the synthesized hydroxyapatite catalysts $Au_{0.8}Pd_{0.2}$/HAP-T showed 94.2%

furfural conversion and 99% methyl 2-furoate selectivity. The replacement of corrosive bases by TBHP in the oxidative esterification of furfural yielded significant results and hence this study proves that such reactions can be performed in a mild and an environmentally benign conditions.

**References**


1. J.P.Lange, E.Heide, J. Buijtenen and R.Price, *Chem. Sus. Chem.*, 2012, **5**, 150-166.
2. D.M.Alonso, J.Q.Bond and J. Dumesic, *Green Chem.*, 2010, **12**, 1493-1513.
3. K.J.Zeitsch, The Chemistry and Technology of furfural and its many by-products, Amsterdam; *Elsevier*, 2000.
4. K.Yan, G.Wu, T. Laufluer and C. Jarvis, *Renew. Sust. Energ. Rev.,* 2014, **38**, 663-676.
5. M. Stocker, *Angew. Chem. Int. Ed*., 2008, **47**, 9200-9211.
6. D.T.Win, Furfural – Gold to Garbage, *AU. J. Technol.*, 2005, **8**, 185-190.
7. G. Ramya, R. Sudhakar, J. Amala Infant Joice, R. Ramakrishnan, T. Sivakumar, *Appl. Catal., A: General*, 2012, **8**, 170-178.
8. G.Ramya, R.Sudhakar, K.Kathiravan and T.Sivakumar, *Advanced Porous Materials*, 2014, **2**,113-123(11).
9. G.Ramya, T. Sivakumar, Mohammad Arif and Zakwan Ahmed, *Energy Sources, Part A: Recovery, Utilization, and Environmental Effects*, 2015, **37**,878–885.
10. G.Ramya, T.Sivakumar, Mohommad Arif and Zakwan Ahmed, *Energy Sources, Part A: Recovery, Utilization, and Environmental Effects*, 2015, **37**, 758–765.
11. K. Triantafyllidis, A. Lappas, M. Stocker, The Role of Catalysis for the Sustainable Production of Bio-Fuels and Biochemicals, *Elsevier*, 2013.

12. E. Taarning, I.S. Nielson, K. Egebled, R. Madson and C.H. Christensen, *Chem. Sus. Chem*., 2008, **1**, 75-78.

13. W. Suchanek and M. Yoshimura, *J. Mater. Res.*, 1998, **13**, 94–117.

14. T. Long, Y.P. Guo, Y.Z. Liu and Z.A.Zhu, *RSC Adv*., 2013, **3**, 24169-24176.

15. J. Kolmas, S. Krukowski, A. Laskus, M. Jurkitewicz, *Ceram. Int.*, 2016, **42**, 2472-2487.

16. T. Matsumoto, M. Okazaki, M. Inoue, S. Yamaguchi, T. Kusunose, T. Toyonaga, Y. Hamada, J. Takahashi, *Biomaterials*, 2004, **25**, 3807–3812.

17. K. Lin, L. Xia, J. Gan, Z. Zhang, H. Chen, X. Jiang and J. Chang, *ACS Appl. Mater. Interfaces*, 2013, **5**, 8008−8017.

18. X.Y.Zhao, Y.J.Zhu, F.Chen, B.Q. Lu and J. Wu , *CrystEngComm*, 2013,**15**, 206-212.

19. K. Kaneda and T. Mizugaki, *Energy Environ. Sci.,* 2009, **2**, 655-673.

20. K. Mori , T. Hara , T. Mizugaki , K. Ebitani , and K. Kaneda, *J. Am. Chem. Soc.*, 2004, **126**, 10657–10666

21. M. Vukomanovic,U. Repnik, T Z.Bergant, R. Kostanjsek, S.D.S Kapin and D. Suvorov, *ACS Biomater. Sci. Eng.*, 2015, **1**,935−946.

22. B. M. Choudary ,C. Sridhar, M. L. Kantam, G. T. Venkanna and B. Sreedhar, *J. Am. Chem. Soc.*, 2005, **127**, 9948–9949.

23. N.Elazarifi, M.A.Chaoui, A.E.Ouassouli, A. Ezzamarty, A. Travert, J. Leglise, L.C. Menorval, C. Moreau, *Catal. Today*, 2004, **98**,161–170.

24. R. Tahir, K. Banert, A. Solhy, S. Sebti, *J. Mol. Catal. A: Chem.*, 2006, **246**, 39-42.

25. D.F. Mercado, G. Magnacca, M. Malandrino, A. Rubert, E. Montoneri, L.Celi, A.B.Prevot, and M. C. Gonzalez, *ACS Appl. Mater. Interfaces*, 2014, **6**, 3937–3946.

26. Z. Opre, T. Mallat, A. Baiker, *J. Catal.,* 2007*,* **245**, 482–486.

27. A. Crosman, G. Gelbard, G. Poncelet, V.I. Parvulescu, *Appl. Catal., A*, 2004, **264**, 23–32.

28. A. E. Porter, N. Patel, J.N. Skepper, S.M. Best, W. Bonfield, *Biomaterials*, 2003, **24**, 4609-4620.

29. F. Menegazzoa, M. Signorettoa, F. Pinna, M. Manzoli, V. Aina, G. Cerrato, F. Boccuzzi, *J. Catal.,* 2014, **309**, 241–247.

30. M. Signoretto, F. Menegazzo, L. Contessotto, F. Pinna, M. Manzoli, F. Boccuzzi, *Applied Catalysis B: Environmental*, 2013, **129**, 287–293.

31. F. Pinnaa, A. Olivoa,V. Trevisana,F. Menegazzoa, M. Signorettoa, M. Manzolic, F. Boccuzzic, *Catal. Today*, 2013, **203**, 196–201.

32. F. Menegazzoa, T. Fantinel, M. Signorettoa, F.Pinna, M. Manzoli, *J. Catal.,* 2013, **326**, 1-8.

33. X. Tong, Z. Lui, L. Yu and Y. Li, *Chem. Commun.*, 2015, **51**, 3674-3677.

34. T. Wei, J. Wang, and D. W. Goodman, *J. Phys. Chem. C*, 2007, **111**, 8781-8788.

35. Y. F. Han, J.H. Wang, D. Kumar, Z. Yan, D.W. Goodman, *J. Catal.,* 2005, **232,** 467–475.

36. Y. Hong, X. Jing, J. Huang, D. Sun, T.O.Wubah, F. Yang, M.Du and Qingbiao, *ACS Sustainable Chem. Eng.*, 2014, **2**, 1752−1759.

37. Y. Feng, H. Yin, D. Gao, A. Wang, L. Shen, M. Meng, *J. Catal.,* 2014, **316**, 67–77.

38. Y. Chen, H. Lim, Q. Tang, Y. Gao, T. Sun, Q. Yan, Y. Yang, *Appl. Catal., A: General*, 2010, **380,** 55–65.

39. D.I. Enache, J.K. Edwards, P. Landon, B. Solsona-Espriu, A.F. Carley, A.A. Herzing, M. Watanabe, C.J. Kiely, D.W. Knight, G.J. Hutchings, *Science*, 2006, **311**, 362–365.

40. H. Chen, Y. Li, F. Zhang, G. Zhang, X. Fan, *J. Mater. Chem.*, 2011, **21**, 17658-17661.

41. J. C. Colmenares, P. Lisowski, D. Łomot, O. Chernyayeva and D. Lisovytskiy, *Chem.Sus.Chem*., 2015, **8**, 1676–1685.

42. R. W. J. Scott, O. M. Wilson, Sang-Keun Oh, E.A. Kenik and R.M. Crooks, *J. Am. Chem. Soc.*, 2004, **126**, 15583 -15591.

43. Y. Shiraishi, D. Ikenaga and N. Toshima, *Aust. J. Chem.*, 2003, 56, 1025 – 1029.

44. S. Nishimura, N. Ikeda, K. Ebitani, *Catal. Today*, 2014, **232**, 89-98.

45. X. Wei, X. F. Yang, A. Q. Wang, L. Li, X.Y. Liu, T. Zhang, C. Y. Mou and J. Li, *Phys. Chem. C*, 2012, **116,** 6222–6232.

46. L. Zhang, A. Wang, J. T. Miller, X. Liu, X. Yang, W. Wang, L. Li, Y. Huang, C. Y. Mou, and T. Zhang, *ACS Catalysis*, 2014, **4,** 1546–1553.

47. B.O.Fowler, *Inorganic Chemistry*, 1974, **13(1)**, 194–207

48. B.O.Fowler, *Inorganic Chemistry*, 1974, **13 (2)**, 207–214

49. JCPDS-ICDD, *The International Centre for Diffraction Data*, 2003.

50. Y. Waseda, E. Matsubara, K. Shinoda, X-Ray diffraction crystallography, *Springer*, 2011.

51. R. Ramakrishnan, P. Wilson, T. Sivakumar, I. Jemina, *Ceram. Int.*, 2013, 39, 3519–3532.

52. J. Zheng, H. Lin, Y. Wang, X. Zheng, X. Duan, Y. Yuan, *J. Catal.*, 2013, **297**, 110–118.

53. Y. Chen, H. Wang, C. Liu, Z. Zeng, H. Zhang, C. Zhau, X. Jia, Y. Yang, *J. Catal.*, 2012, **289**, 105-117.

54. A. Q. Wang, J. H. Liu, S.D. Lin, T. S. Lin, C. Y. Mou, *J. Catal.*, 2005, **233**, 186–197.

55. C. Corti, R. Holliday, Gold: Science and Applications, *CRC Press*, 2009.

56. C. Kan, W. Cai, C. Li, L. Zhang and H. Hofmeister, *J. Phys. D: Appl. Phys.*, 2003, **36**, 1609–1614.

57. S. Deki, K. Akamatsu, Y. Hatakenaka, M. Mizuhata and A. Kajinami, *Nano struct. Mater*, 1999, **11**, 59–65.

58. M. L. Wu, D. H. Chen, T. C. Huang, *Langmuir*, 2001, **17**, 3877-3883.

59. Y. W. Lee, N. H. Kim, K. Y. Lee, K. Kwon, M. Kim, and S. W. Han, *J. Phys. Chem. C*, 2008, **112**, 6717-6722.

60. R. W. J. Scott, O. M. Wilson, S. K. Oh, E. A. Kenik and R. M. Crooks, *J. Am. Chem. Soc.,* 2004, **126**, 15583-15591.

61. Y. Chen, H. Lim, Q. Tang, Y. Gao, T. Sun, Q. Yan, Y. Yang, *Appl. Catal., A*: *General*, 2010, **380**, 55-65.

62. J. A. Rodriguez, *Surf. Sci. Rep.*, 1996, **24**, 223-287.

63. Y. Ding, F. Fan, Z. Tian and Z. Lin Wang, *J. Am. Chem. Soc.,*2010, **132**, 12480–12486.

64. N. R. Jana, L. Gearheart, C.J. Murphy, *Chem. Commun.,* 2001, **7**, 617–618.

65. M. P. Mallin and C. J. Murphy, *Nano Letters*, 2002, **2**, 1235-1237.

66. C. Wang, H. Yin, R. Chan, S. Peng, S. Da, S. Sun*, Chem. Mater.*, 2009, **3**, 433-435.

67. D. Wang, Y. Li, *Adv. Mater.*, 2011, **23**, 1044–1060.

68. P. Raveendran, J. Fu, S.L. Wallen, *Green Chem.*, 2006, **8**, 34-38.

69. J. H. Hodak, A. Henglein, M. Giersig, G.V. Hartland, *J. Phys. Chem. B*, 2000, **104**, 11708–11718.

70. S. Pande, S.K. Ghosh, S. Praharaj, S. Panigrahi, S. Basu, S. Jana, A. Pal, T. Tsukuda, *J. Phys. Chem. C*, 2007, **111**,10806-10813.

71. H. Zhang, J. Okuni, N. Toshima, *J. Colloid Interface Sci.*, 2011, **354,** 131–138.

72. S. P. Chandran, J. Ghatak, P.V. Satyam, M. Sastry, *J. Colloid Interface Sci.*, 2007, **312**, 498.

73. H. Zhanga, N. Toshima, *Appl. Catal., A: General*, 2012, **447–448**, 81–88.

74. H.J. Zhang, J. Okuni, N. Toshima, *J. Colloid Interface Sci.,* 354 (2011)131–138.

75. F. Zeng, J. Wang, Y. Wu, Y. Yu, W. Tang, M. Yin, C. Liu, *Colloids and Surfaces A: Physicochem. Eng. Aspects*, 2014, **441**, 737–743.

76. P. Yang, Z. Quan, C. Li, X. Kang, H. Lian, J. Lin, *Biomaterials*, 2008, **29**, 4341–4347.

77. F. Ye, H. Guo, H. Zhang, X. He, *Acta Biomaterialia*, 2010, **6**, 2212–2218.

78. J. F. Moulder, W. F. Stickle, P. E. Sobol, and K. Bomben (J. Chastain, editor), *Handbook of X-ray Photoelectron Spectroscopy 2nd ed., Perkin-Elmer Corporation (Physical Electronics)*, 1992.

79. C. C. Chusuei, D. W. Goodman, M. J. V. Stipdonk, D. R. Justes, and E. A. Schweikert, *Anal. Chem.,* 1999, **71**, 149-153.

80. H. B. Lu, C. T. Campbell, D. J. Graham, B. D. Ratner, *Anal. Chem.* 2000, **72**, 2886-2894.

81. J. Zheng, H. Lin, Y. Wang, X. Zheng, X. Duan, Y. Yuan, *J. Catal.*, 2013, **297**, 110–118.

82. C. W. Yi, K. Luo, T. Wei and D. W. Goodman, The composition and structure of Pd–Au surfaces, *J. Phys. Chem. B*, 2005,**109**, 18535.

83. F. Gao, D. W. Goodmanz, Chem. Soc. Rev., 2012, **41**, 8009–8020.

84. H. Wang, C. Wang, H. Yan, H. Yi, J. Lu, *J. Catal.*, 2015, **324**, 59–68.

85. S. Nishimura, Y. Yakita, M. Katayama, K. Higashimine, K. Ebitani, *Catal. Sci. Technol*., 2013, **3**, 351-359.

86. S. Nishimura, N. Ikeda, K. Ebatani, *Catal. Today*, 2014, **232**, 89-98.

87. H. Chen, Y. Li, F. Zhang, G. Zhang, X. Fan, *J. Mater. Chem*., 2011, **21**, 17685-17661.

88. F. Chen, P. Huang, Y. J. Zhu, J. Wu, C. L. Zhang, D. X. Cui, *Biomaterials*, 2011, **32**, 9031-9039.

## FIGURE CAPTIONS

**Fig.1.** Small angle x-ray powder diffraction pattern of hydroxyapatite (HAP-T) catalyst.

**Fig.2.**Wide angle x-ray powder diffraction pattern of hydroxyapatite (HAP-T) catalyst.

**Fig.3.** Wide angle x-ray powder diffraction pattern of (a) Au/HAP-T, (b) $Au_{0.8}Pd_{0.2}$/HAP-T (c) $Au_{0.6}Pd_{0.4}$/HAP-T, (d) $Au_{0.4}Pd_{0.6}$/HAP-T, (e) $Au_{0.2}Pd_{0.8}$/HAP-T and (f) Pd/HAP-T. (H-Hydroxyapatite, A- Gold, P-Palladium).

**Fig.4.** Wide angle x-ray powder diffraction pattern of (a) $Au_{0.8}Ag_{0.2}$/HAP-T, (b) $Au_{0.6}Ag_{0.4}$/HAP-T, (c) $Au_{0.4}Ag_{0.6}$/HAP-T, (d) $Au_{0.2}Ag_{0.8}$/HAP-T and (e) Ag/HAP-T. (H-Hydroxyapatite, A- Gold & Silver).

**Fig.5.** UV-DRS spectra of (a) Au/HAP-T, (b) $Au_{0.8}Pd_{0.2}$/HAP-T, (c) $Au_{0.6}Pd_{0.4}$/HAP-T, (d) $Au_{0.4}Pd_{0.6}$/HAP-T, (e) $Au_{0.2}Pd_{0.8}$/HAP-T and (f) Pd/HAP-T.

**Fig.6.** UV-DRS spectra of (a) HAP-T, (b)Au/HAP-T, (c) $Au_{0.8}Ag_{0.2}$/HAP-T, (d) $Au_{0.6}Ag_{0.4}$/HAP-T, (e) $Au_{0.4}Ag_{0.6}$/HAP-T, (f) $Au_{0.2}Ag_{0.8}$/HAP-T and (g) Ag/HAP-T.

**Fig.7.** Nitrogen adsorption –desorption isotherm of bare HAP-T.

**Fig.8.** Pore size distribution of bare HAP-T calculated from the desorption branch using BJH algorithm.

**Fig.9.** Overall XPS survey spectra of Au-HAP-T catalyst.

**Fig.10.** XPS spectra of Au4f ($Au4f_{7/2}$ & $Au4f_{5/2}$), Pd3d ($Pd3d_{3/2}$ & $Pd3d_{5/2}$) & ($Ag3d_{3/2}$ & $Ag3d_{5/2}$) core levels of the catalysts (a) Au/HAP-T (b) Ag/HAP-T and (c) Pd/HAP-T.

**Fig.11.** XPS spectra in the of Au($Au4f_{7/2}$ & $Au4f_{5/2}$) and Ag($Ag_{3/2}$ & $Ag3d_{5/2}$) core levels for the catalysts (a) $Au_{0.8}Ag_{0.2}$/HAP-T, (b) $Au_{0.6}Ag_{0.4}$/HAP-T, (c) $Au_{0.8}Ag_{0.2}$/HAP-T and (d) $Au_{0.8}Ag_{0.2}$/HAP-T.

**Fig.12.** XPS spectra of Au4f ($Au4f_{7/2}$ & $Au4f_{5/2}$) and Pd3d ($Pd3d_{3/2}$ & $Pd3d_{5/2}$) core levels of the bimetallic catalysts (a) $Au_{0.8}Pd_{0.2}$/HAP-T, (b) $Au_{0.6}Pd_{0.4}$/HAP-T, (c) $Au_{0.4}Pd_{0.6}$/HAP-T and (d) $Au_{0.2}Pd_{0.8}$/HAP-T.

**Fig.13.** (a) HR-SEM images of bare HAP-T at Low magnification (b) High magnification and its HR-TEM images (c) 200nm magnification (d) 20nm magnification (e) 5nm magnification and its (f) SAED pattern.

**Fig.14.** HR-TEM images of Au/HAP-T (a, d), Ag/HAP-T (b, e) and Pd/HAP-T (c, f) catalysts with magnification at 20nm and 5nm.

**Fig.15.** HR-TEM images of $Au_{0.8}Pd_{0.2}$/HAP-T (a-e) and $Au_{0.6}Pd_{0.4}$/HAP-T (f) catalysts.

**Fig.16.** Effect of recyclability of $Au_{0.8}Pd_{0.2}$/HAP-T on conversion and selectivity in the oxidative esterification of furfural..

## TABLE CAPTIONS

**Table.1** Average particle size of different hydroxyapatite as calculated by XRD and HR-TEM studies.

**Table.2** d-spacing and lattice parameter values of mono and bimetallic hydroxyapatites.

**Table.3.** Surface metal concentration and binding energy values of mono (Au or Pd) and bimetallic hydroxyapatites (Au & Pd).

**Table.4** Surface metal concentration and binding energy values of mono (Au or Ag) and bimetallic hydroxyapatites (Au & Ag).

**Table.5** Effect of temperature on the conversion of furfural and selectivity towards methyl 2-furoate.

**Table.6** Oxidative esterification of furfural to methyl 2-furoate over mono (Au or Pd) and bimetallic hydroxyapatites (Au and Pd).

**Table.7** Oxidative esterification of furfural to methyl 2-furoate over mono (Au or Ag) and bimetallic hydroxyapatites (Au and Ag).

**Table.8** Effect of air, oxygen and bases on conversion and selectivity in the oxidative esterification of furfural.

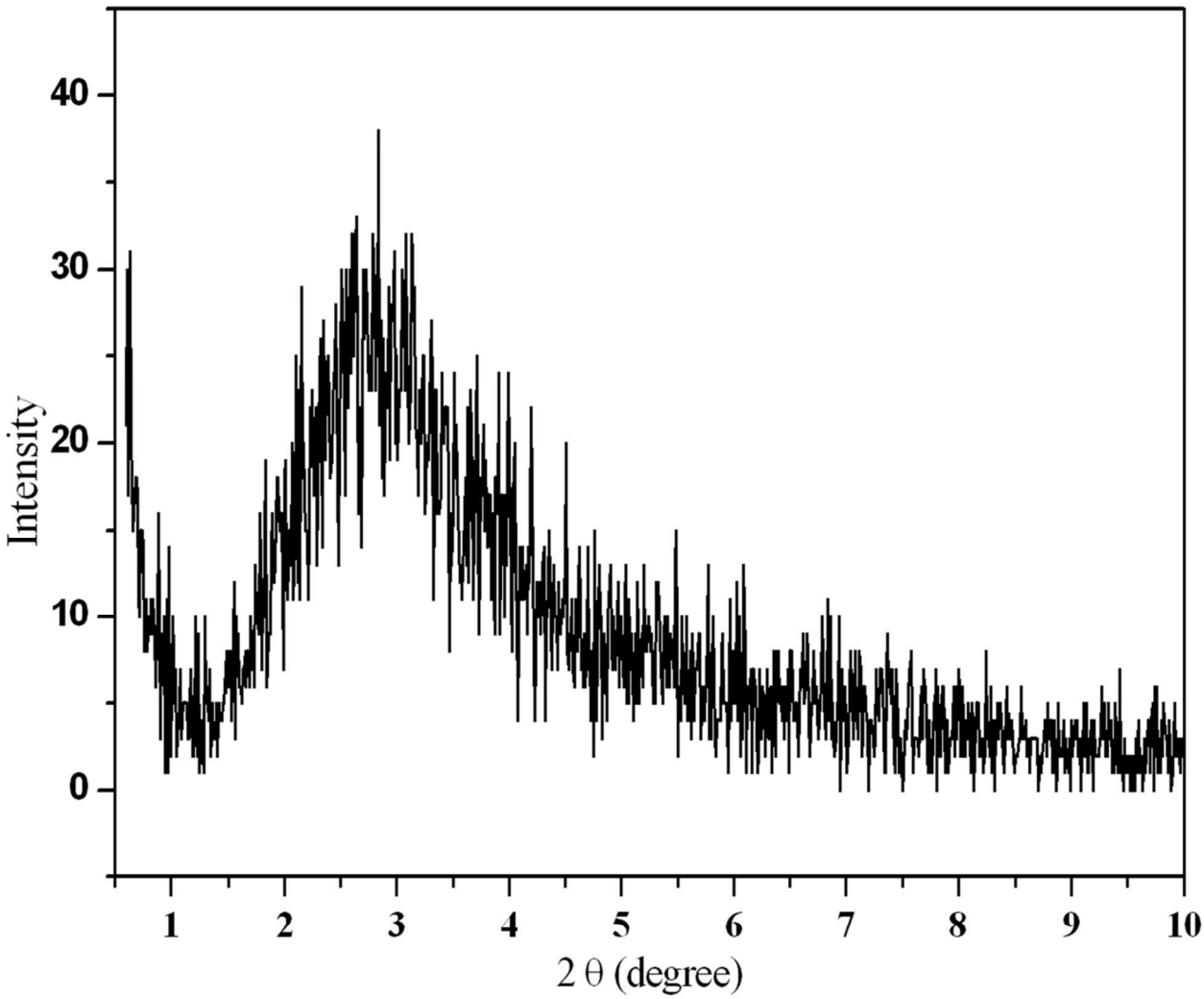


**Fig.1.** Small angle x-ray powder diffraction pattern of hydroxyapatite (HAP-T) catalyst.

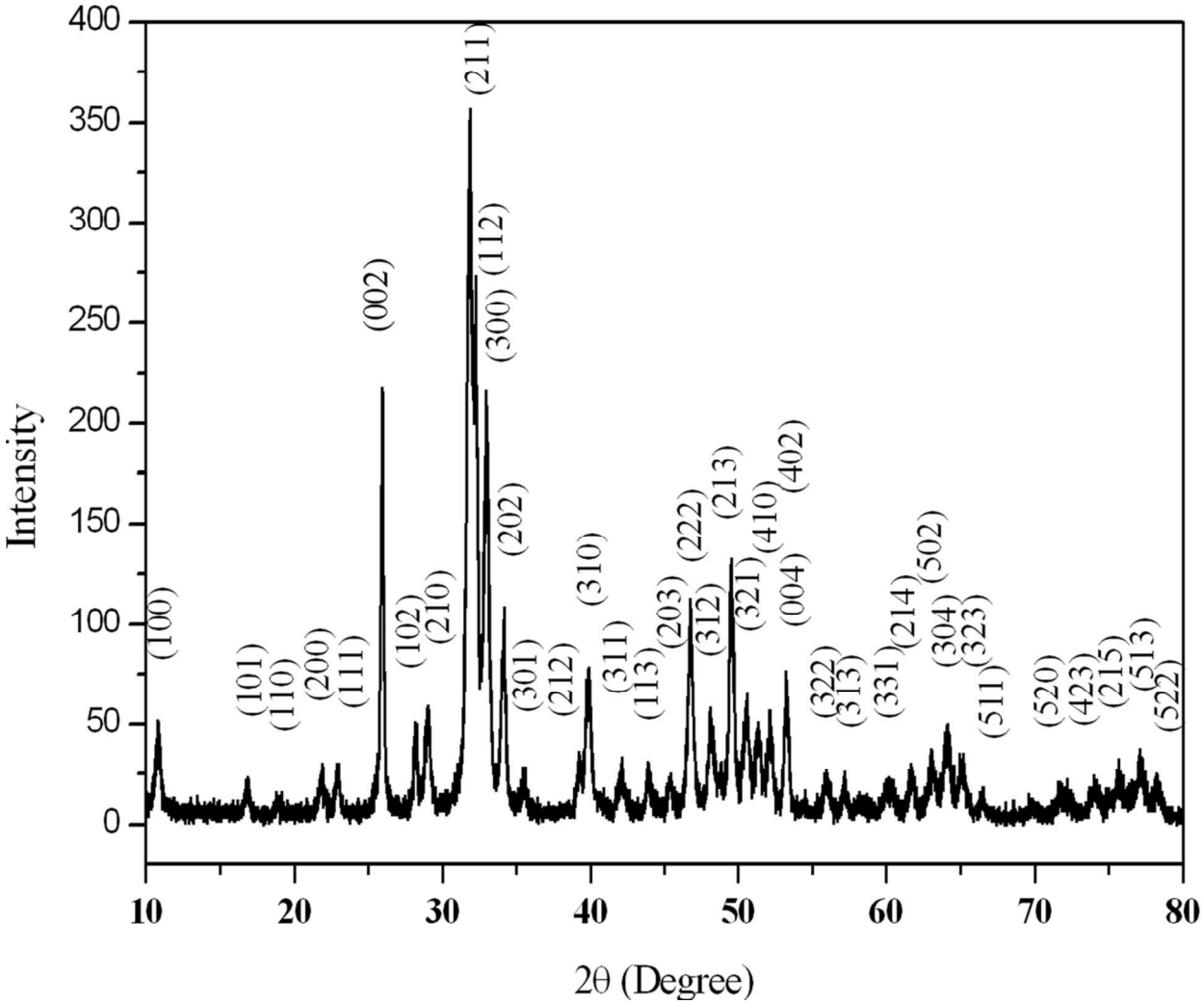


**Fig.2.**Wide angle x-ray powder diffraction pattern of hydroxyapatite (HAP-T) catalyst.

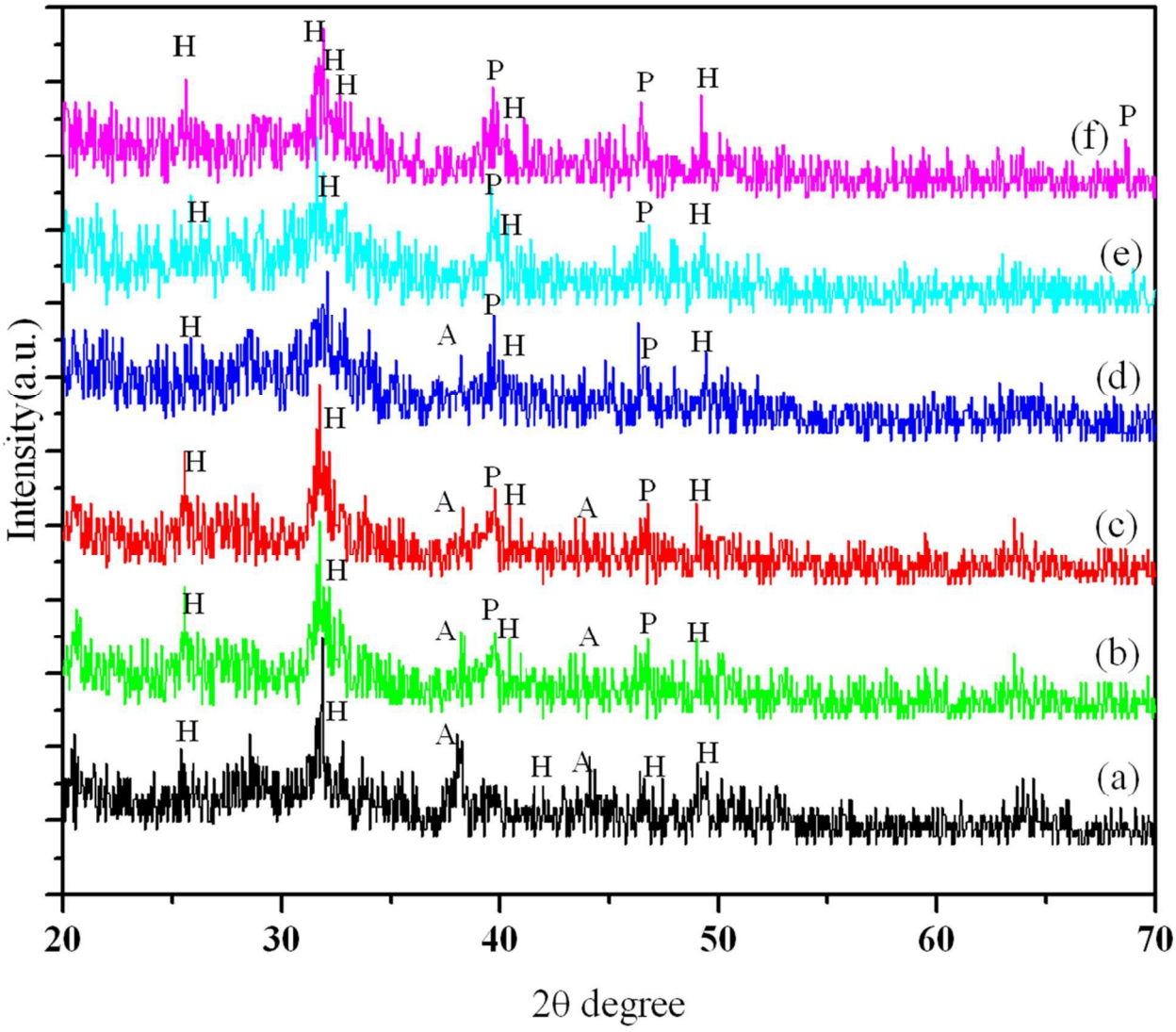


**Fig.3**. Wide angle x-ray powder diffraction pattern of (a). Au/HAP-T (b). $Au_{0.8}Pd_{0.2}$/HAP-T (c). $Au_{0.6}Pd_{0.4}$/HAP-T (d). $Au_{0.4}Pd_{0.6}$/HAP-T (e) $Au_{0.2}Pd_{0.8}$/HAP-T and (f). Pd/HAP-T. (H-Hydroxyapatite, A- Gold, P-Palladium).

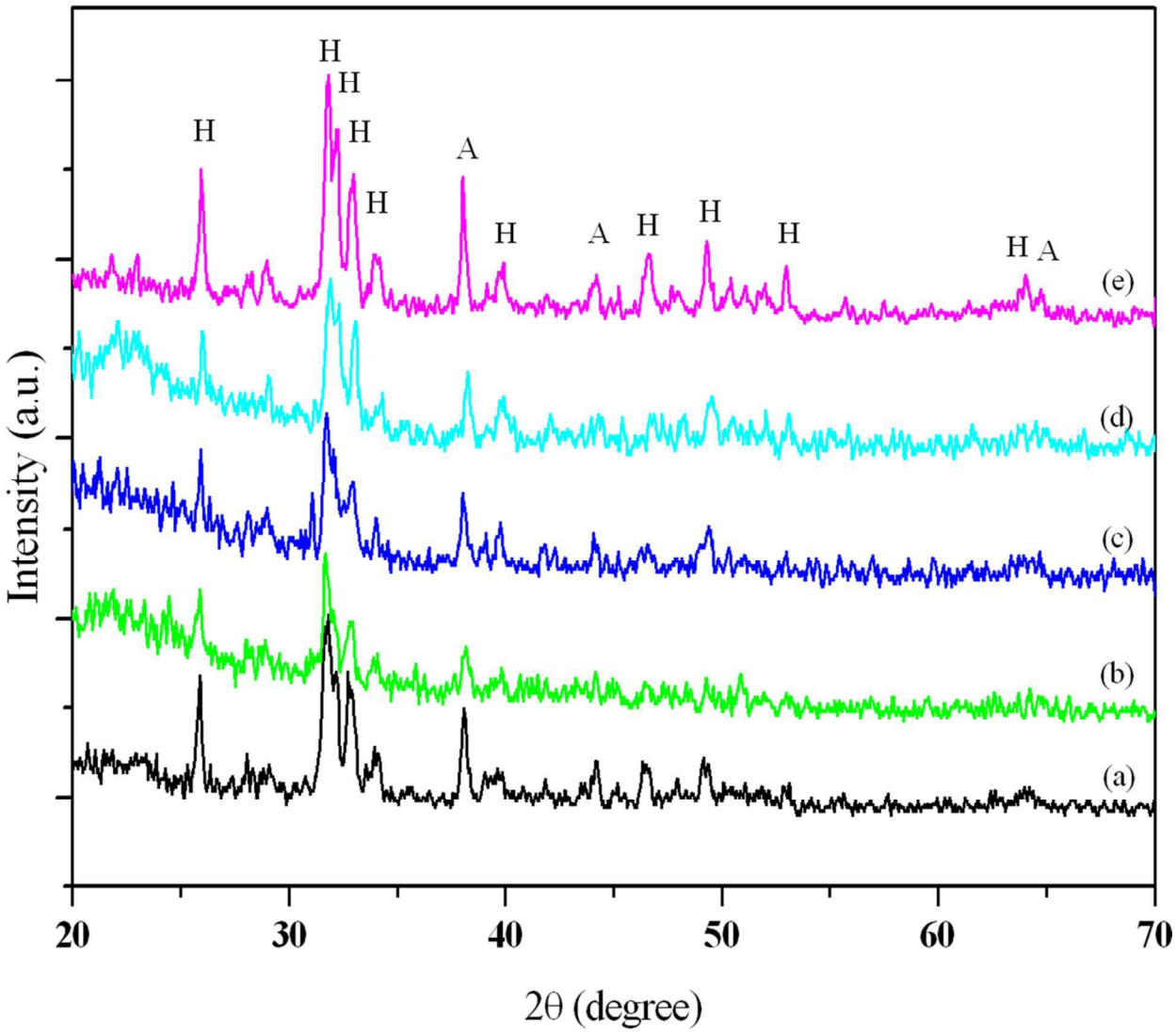


**Fig.4.**Wide angle x-ray powder diffraction pattern of (a). $Au_{0.8}Ag_{0.2}$/HAP-T (b). $Au_{0.6}Ag_{0.4}$/HAP-T (c). $Au_{0.4}Ag_{0.6}$/HAP-T (d) $Au_{0.2}Ag_{0.8}$/HAP-T and (e). Ag/HAP-T. (H-Hydroxyapatite, A- Gold & Silver).

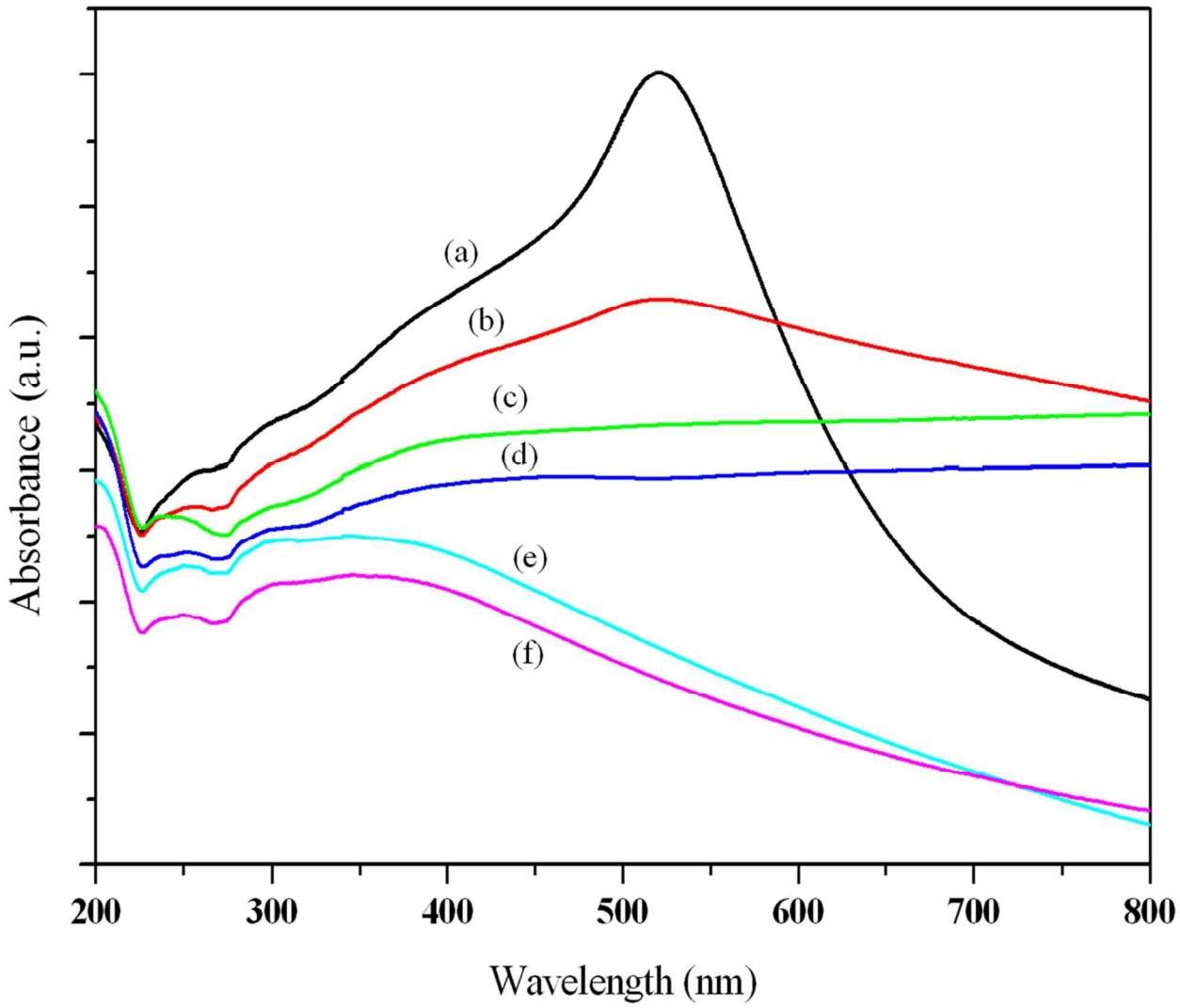


**Fig.5**. UV-DRS spectra of (a). Au/HAP-T (b). $Au_{0.8}Pd_{0.2}$/HAP-T (c). $Au_{0.6}Pd_{0.4}$/HAP-T (d). $Au_{0.4}Pd_{0.6}$/HAP-T (e) $Au_{0.2}Pd_{0.8}$/HAP-T and (f). Pd/HAP-T.

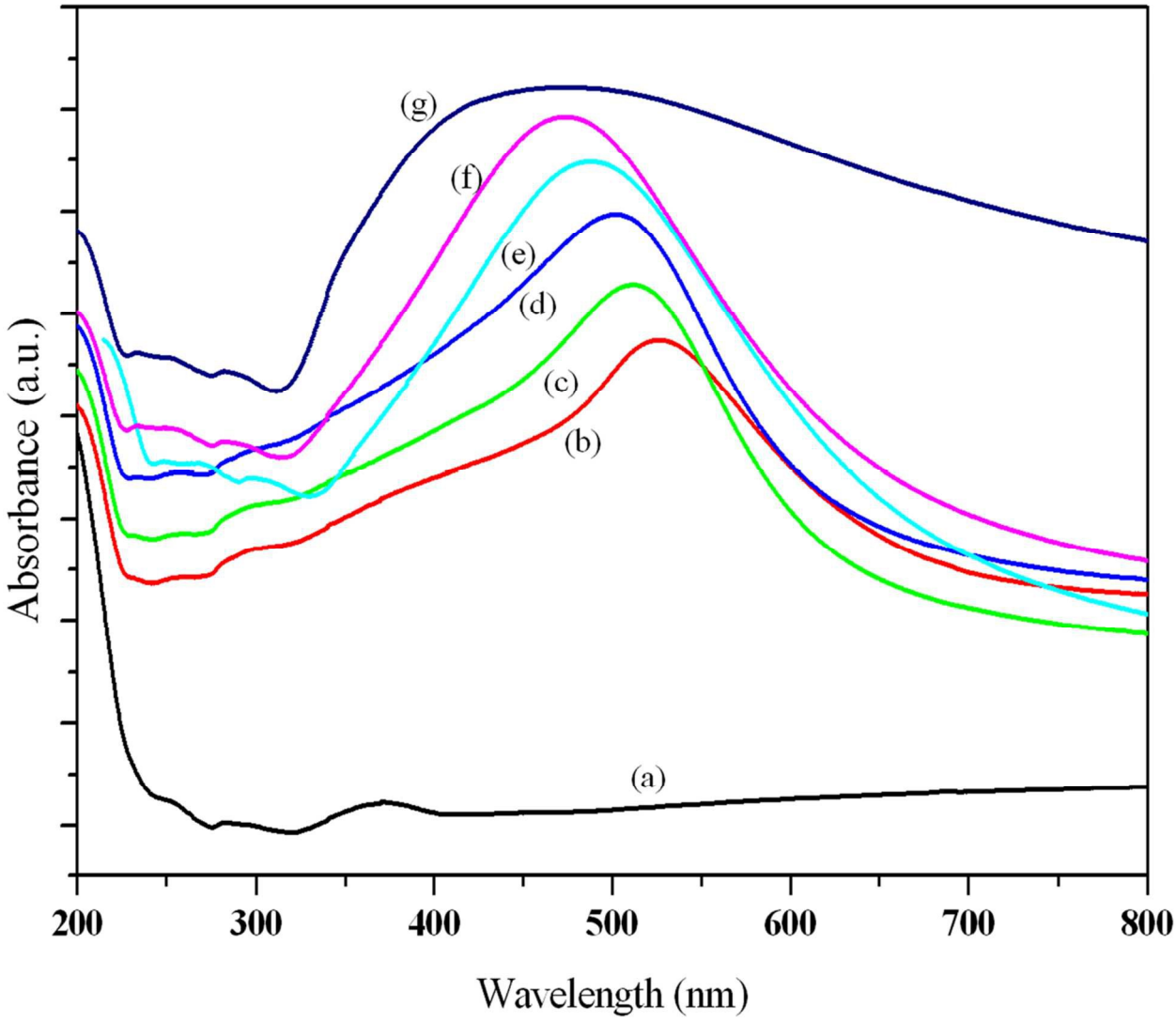


**Fig.6.** UV-DRS spectra of (a). HAP-T (b). Au/HAP-T (c). $Au_{0.8}Ag_{0.2}$/HAP-T (d). $Au_{0.6}Ag_{0.4}$/HAP-T (e). $Au_{0.4}Ag_{0.6}$/HAP-T (f) $Au_{0.2}Ag_{0.8}$/HAP-T, and (g). Ag/HAP-T.

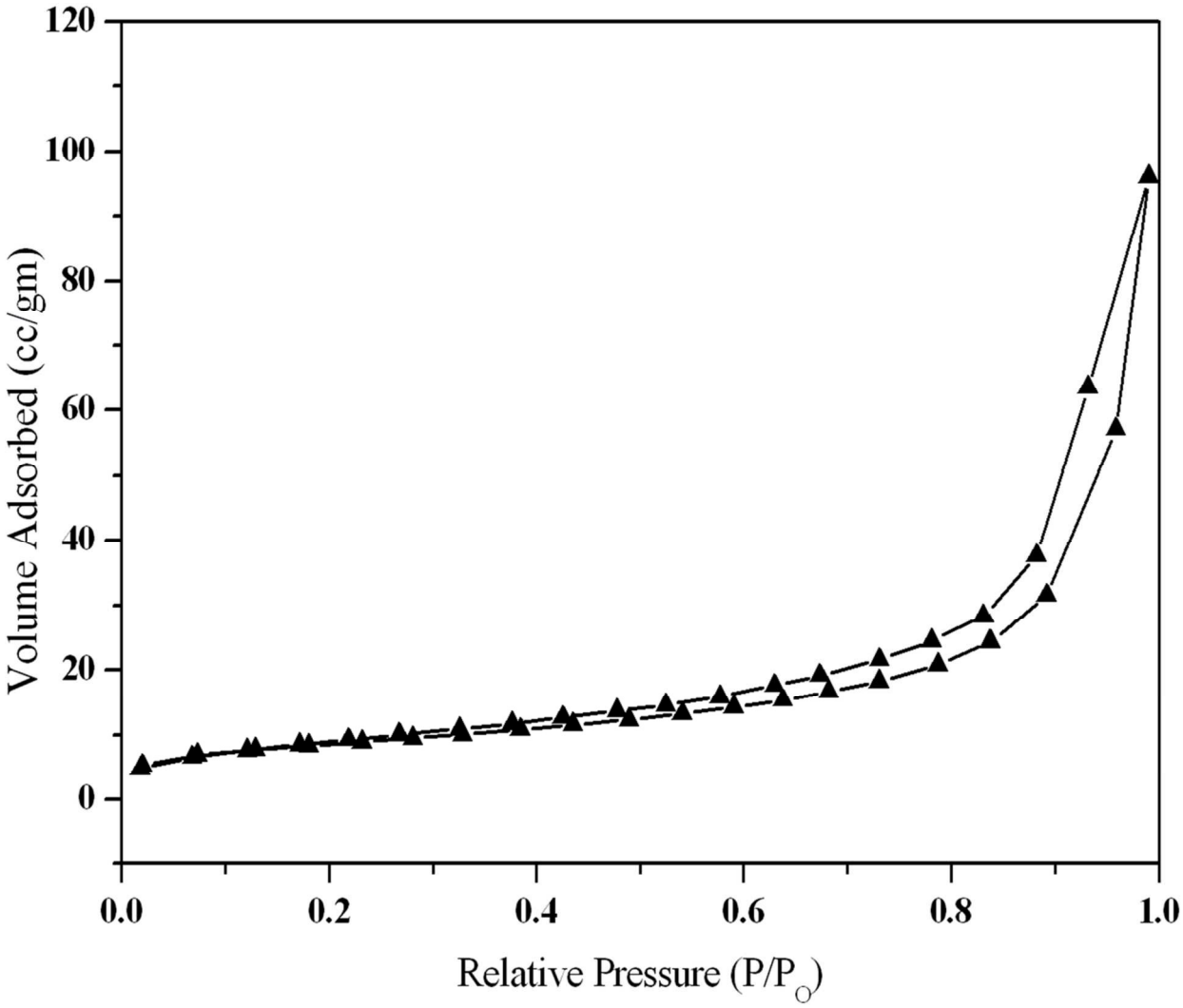


**Fig.7.** Nitrogen adsorption –desorption isotherm of bare HAP-T

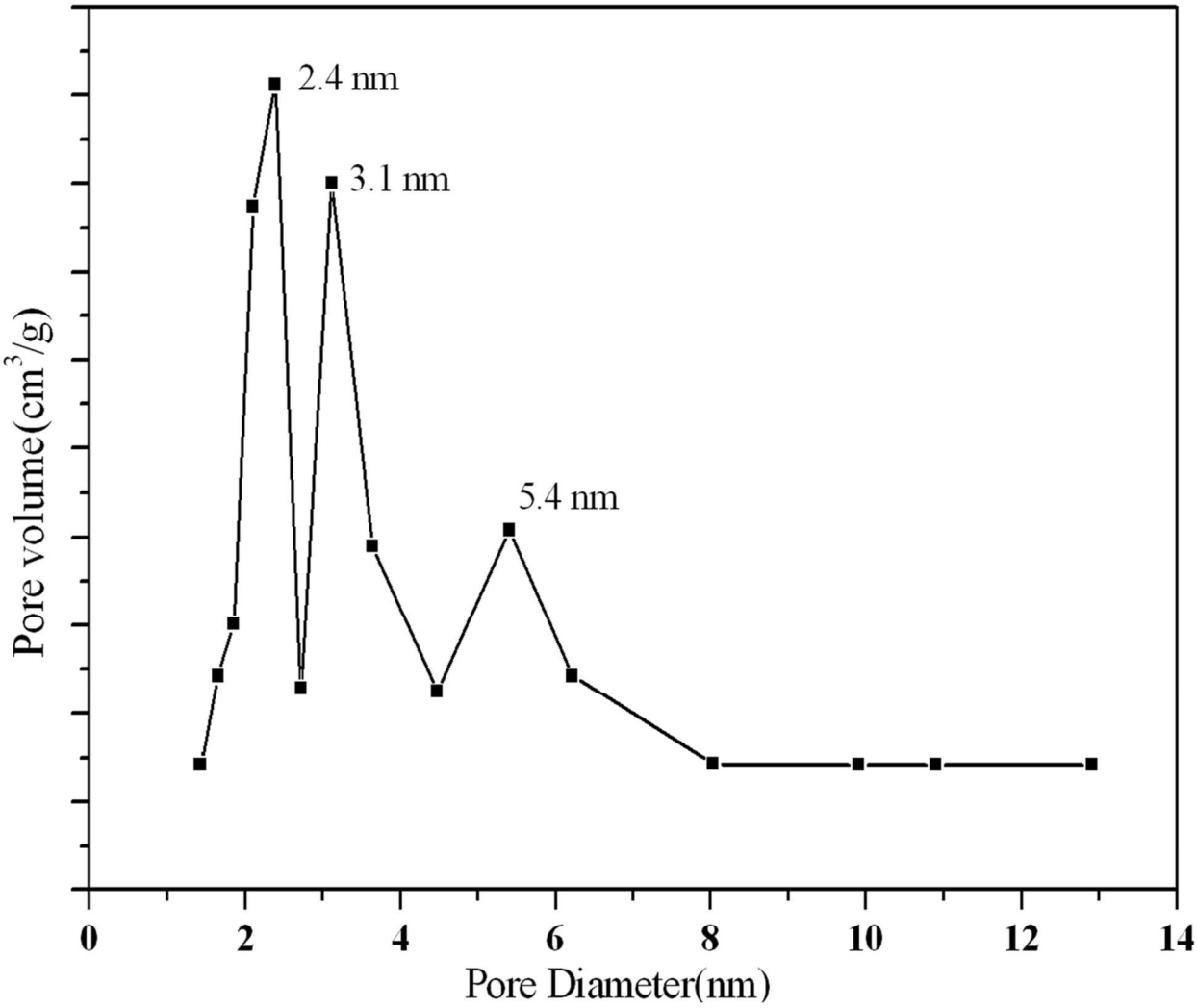


**Fig.8.** Pore size distribution of bare HAP-T calculated from the desorption branch using BJH algorithm.

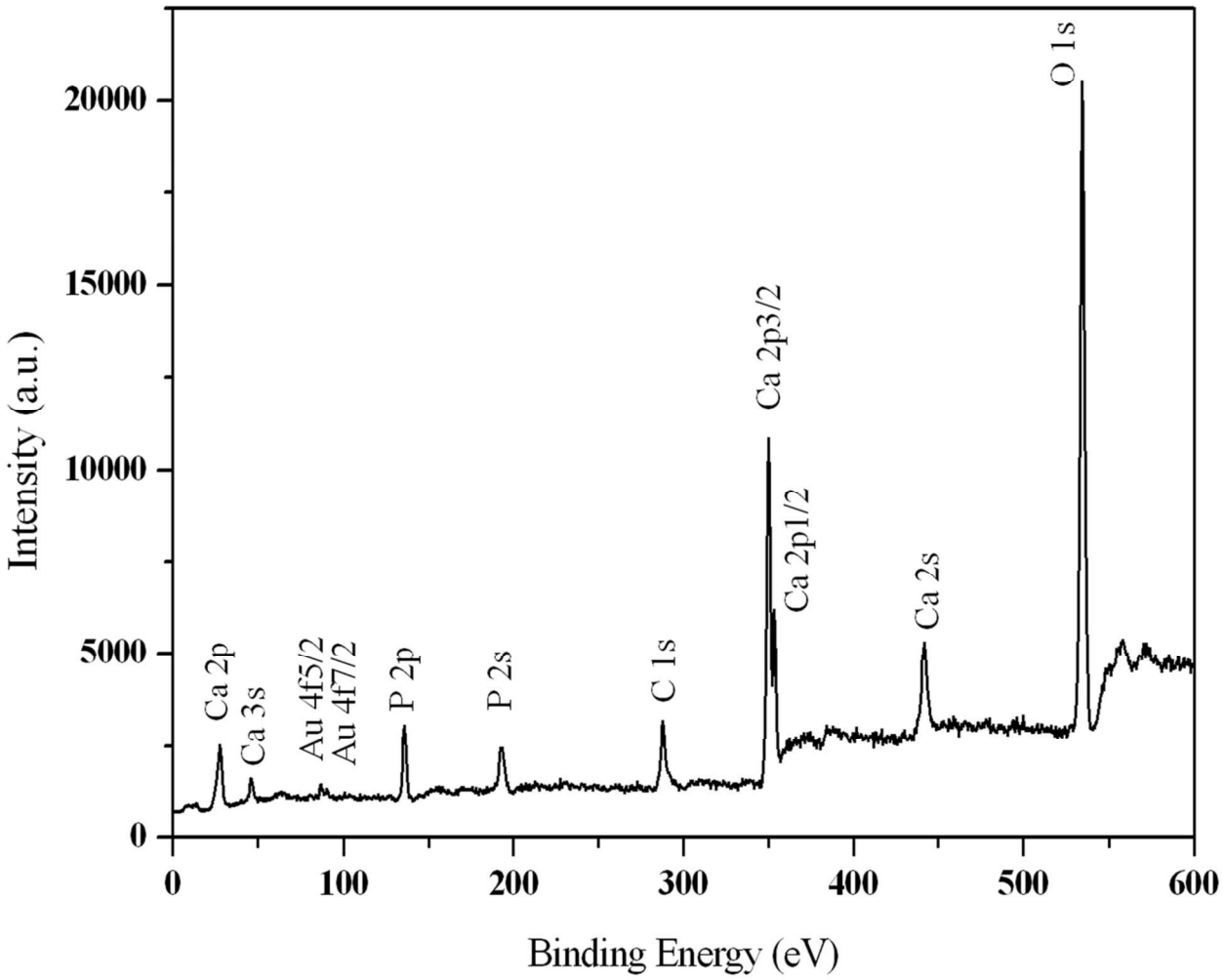


**Fig.9.** Overall XPS survey spectra of Au-HAP-T catalyst.

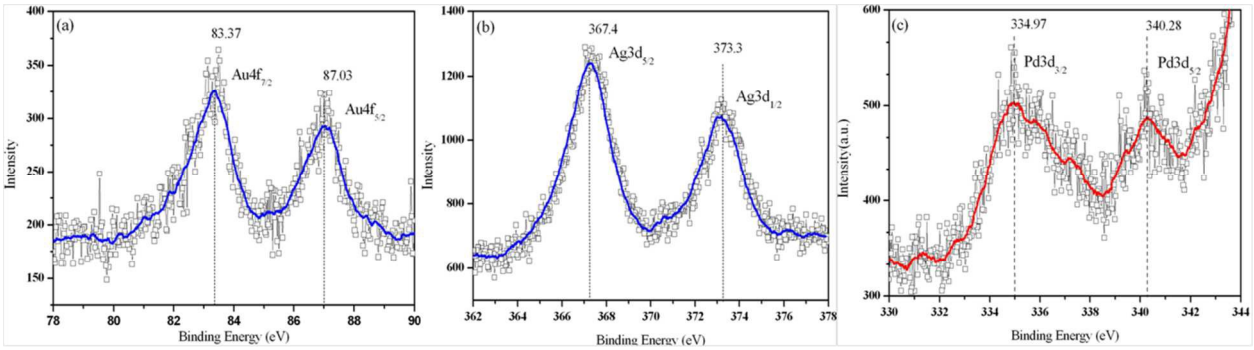


**Fig.10**. XPS spectra of $Au_{4f}$ ($Au_{4f7/2}$ & $Au_{4f5/2}$), $Pd_{3d}$ ($Pd_{3d3/2}$ & $Pd_{3d5/2}$) & ($Ag_{3d3/2}$ & $Ag_{3d5/2}$) core levels of the catalysts (a). Au/HAP-T (b). Ag/HAP-T and (c). Pd/HAP-T.

**(a) $Au_{0.8}Ag_{0.2}$/HAP-T**

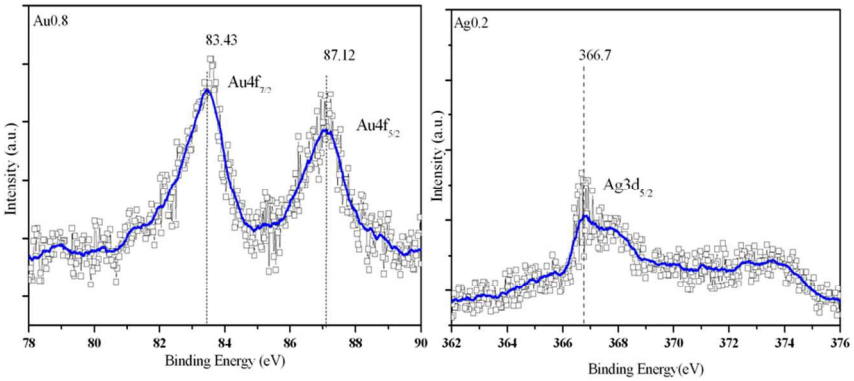


**(b) $Au_{0.6}Ag_{0.4}$/HAP-T**

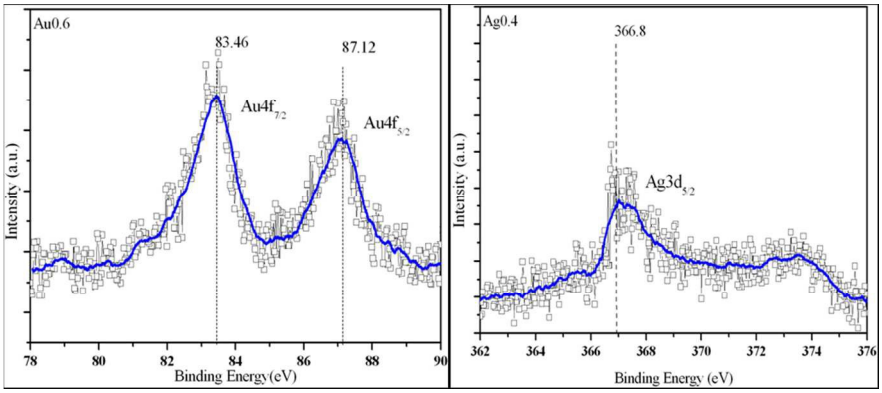


**(c) $Au_{0.4}Ag_{0.6}$/HAP-T**

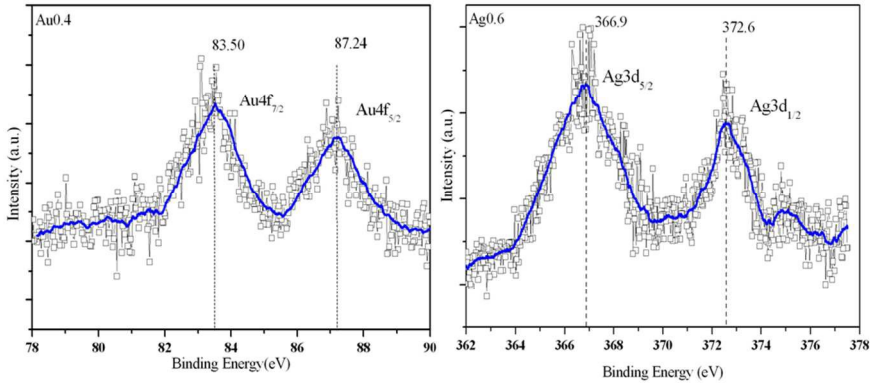


**(d) $Au_{0.2}Ag_{0.8}$/HAP-T**

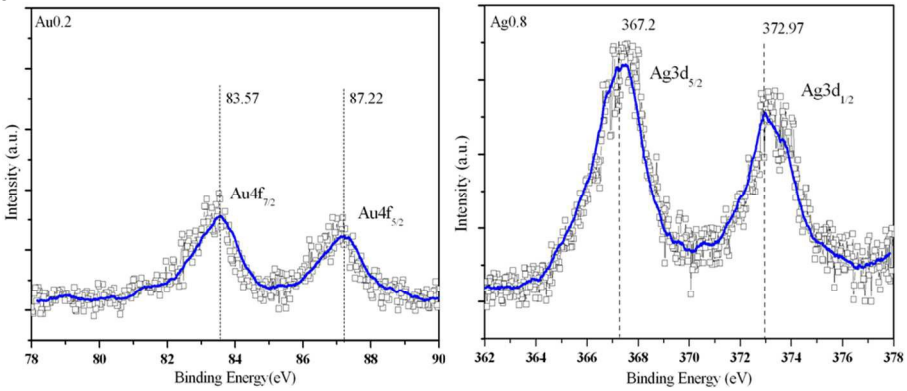


**Fig.11.** XPS spectra in the of Au($Au4f_{7/2}$ & $Au4f_{5/2}$) and Ag($Ag_{3/2}$ & $Ag3d_{5/2}$) core levels for the catalysts (a) $Au_{0.8}Ag_{0.2}$/HAP-T, (b) $Au_{0.6}Ag_{0.4}$/HAP-T, (c) $Au_{0.8}Ag_{0.2}$/HAP-T and (d) $Au_{0.8}Ag_{0.2}$/HAP-T.

**(a) $Au_{0.8}Pd_{0.2}$/HAP-T**

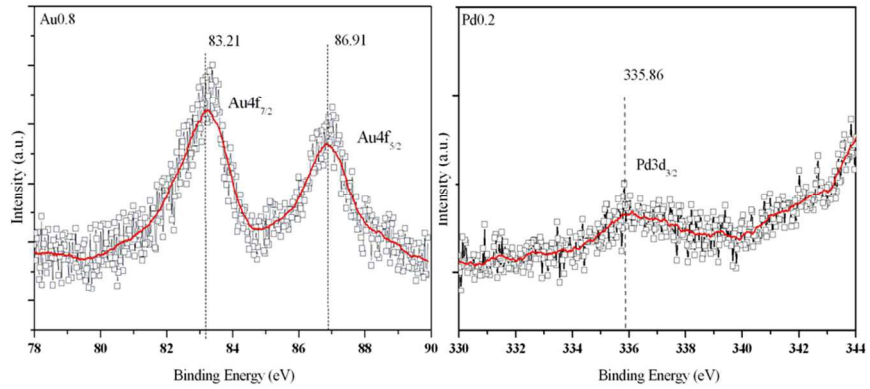


**(b) $Au_{0.6}$ $Pd_{0.4}$/HAP-T**

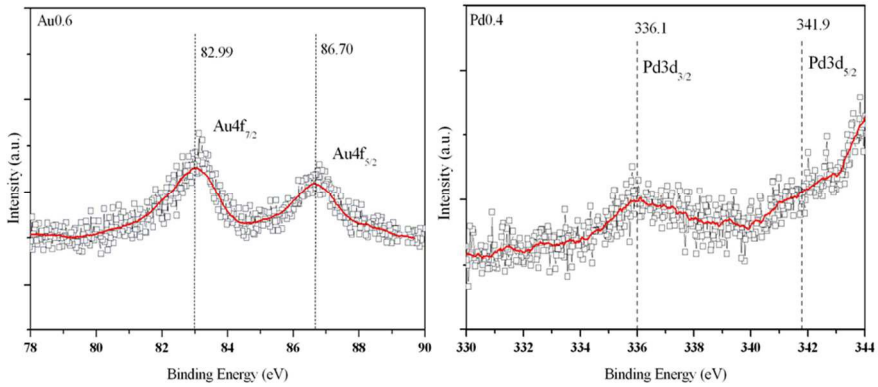


**(c) $Au_{0.4}$ $Pd_{0.6}$/HAP-T**

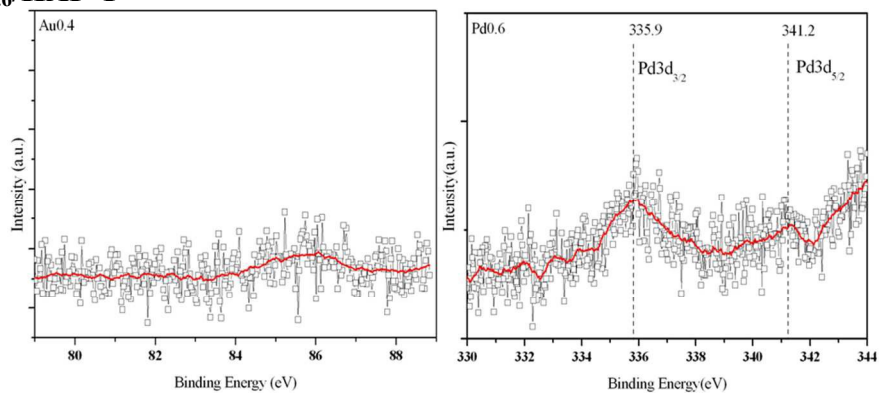


**(d) $Au_{0.2}$ $Pd_{0.8}$/HAP-T**

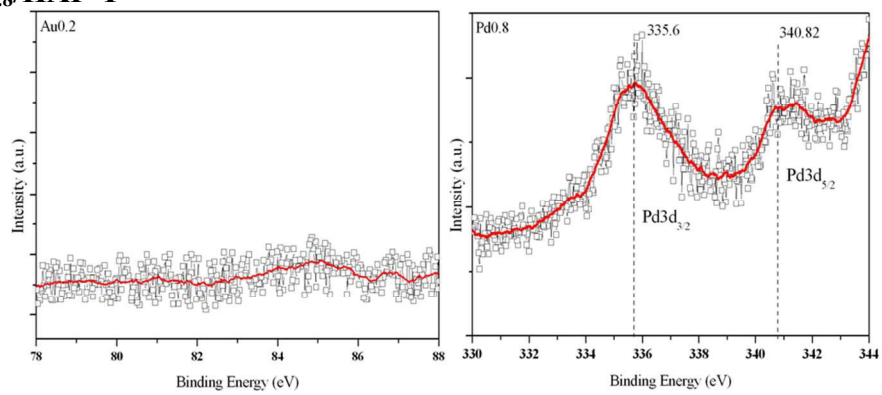


**Fig.12.** XPS spectra of $Au_{4f}$ ($Au_{4f7/2}$ & $Au_{4f5/2}$) and $Pd_{3d}$ ($Pd_{3d3/2}$ & $Pd_{3d5/2}$) core levels of the bimetallic catalysts (a).$Au_{0.8}Pd_{0.2}$/HAP-T (b). $Au_{0.6}Pd_{0.4}$/HAP-T (c). $Au_{0.4}Pd_{0.6}$/HAP-T and (d) $Au_{0.2}Pd_{0.8}$/HAP-T;

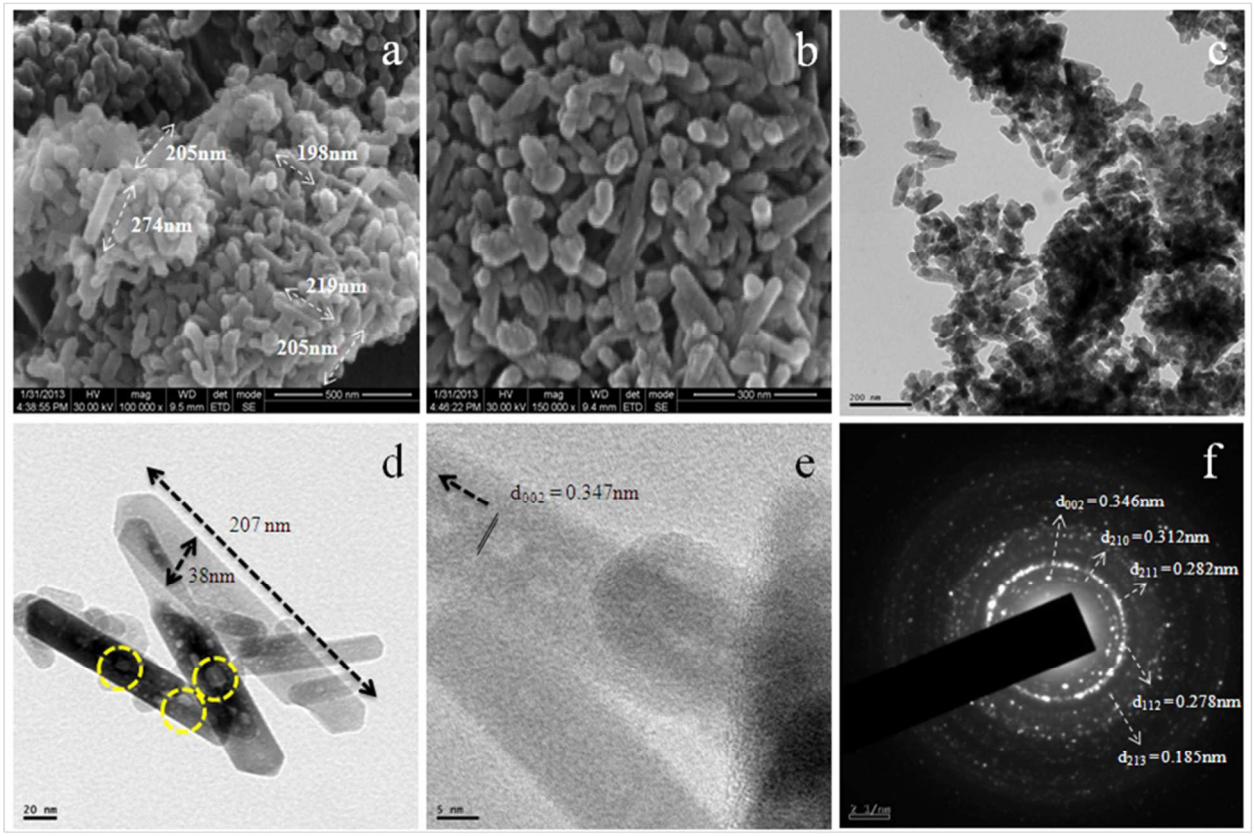


**Fig.13. (a)** HR-SEM images of bare HAP-T at Low magnification **(b)** High magnification and its HR-TEM images **(c)** 200nm magnification (d) 20nm magnification **(e)** 5nm magnification and its **(f)** SAED pattern.

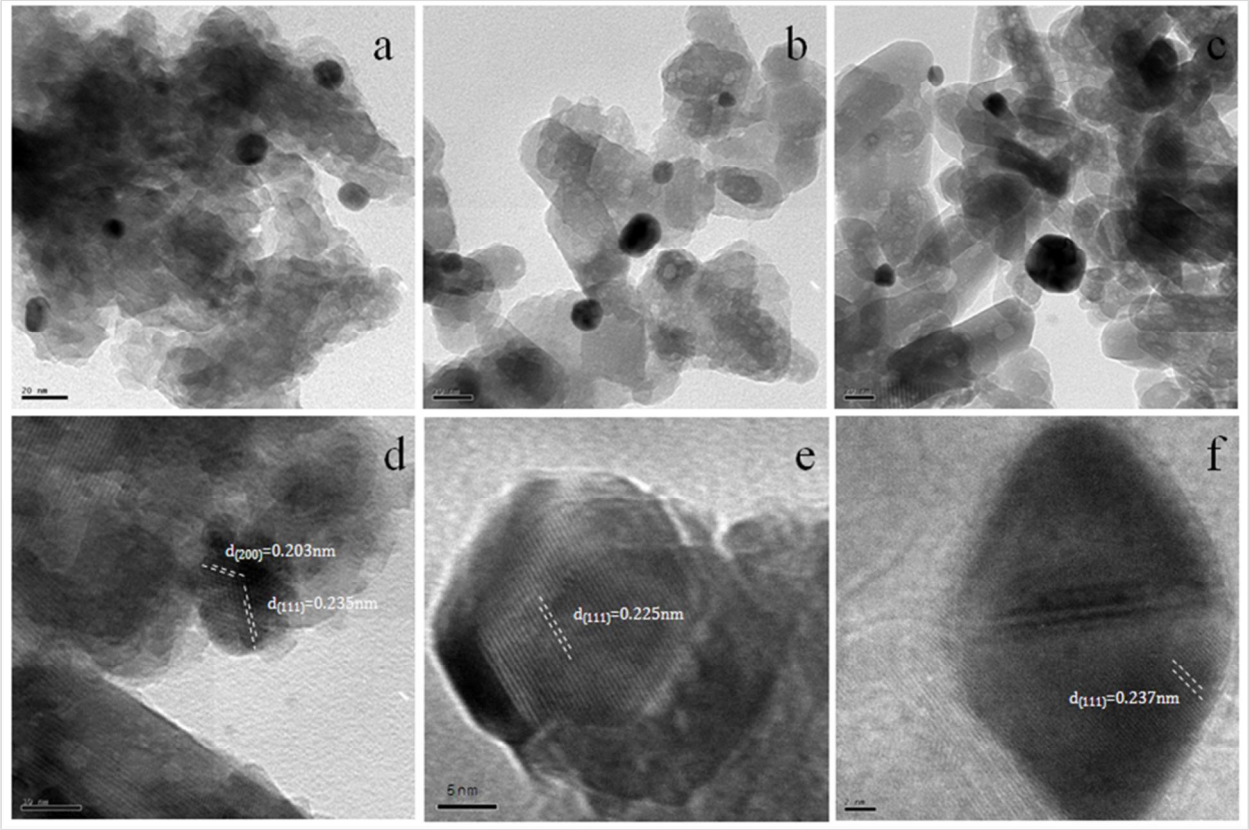


**Fig.14.** HR-TEM images of Au/HAP-T (a, d), Ag/HAP-T (b, e) and Pd/HAP-T (c, f) catalysts with magnification at 20nm and 5nm.

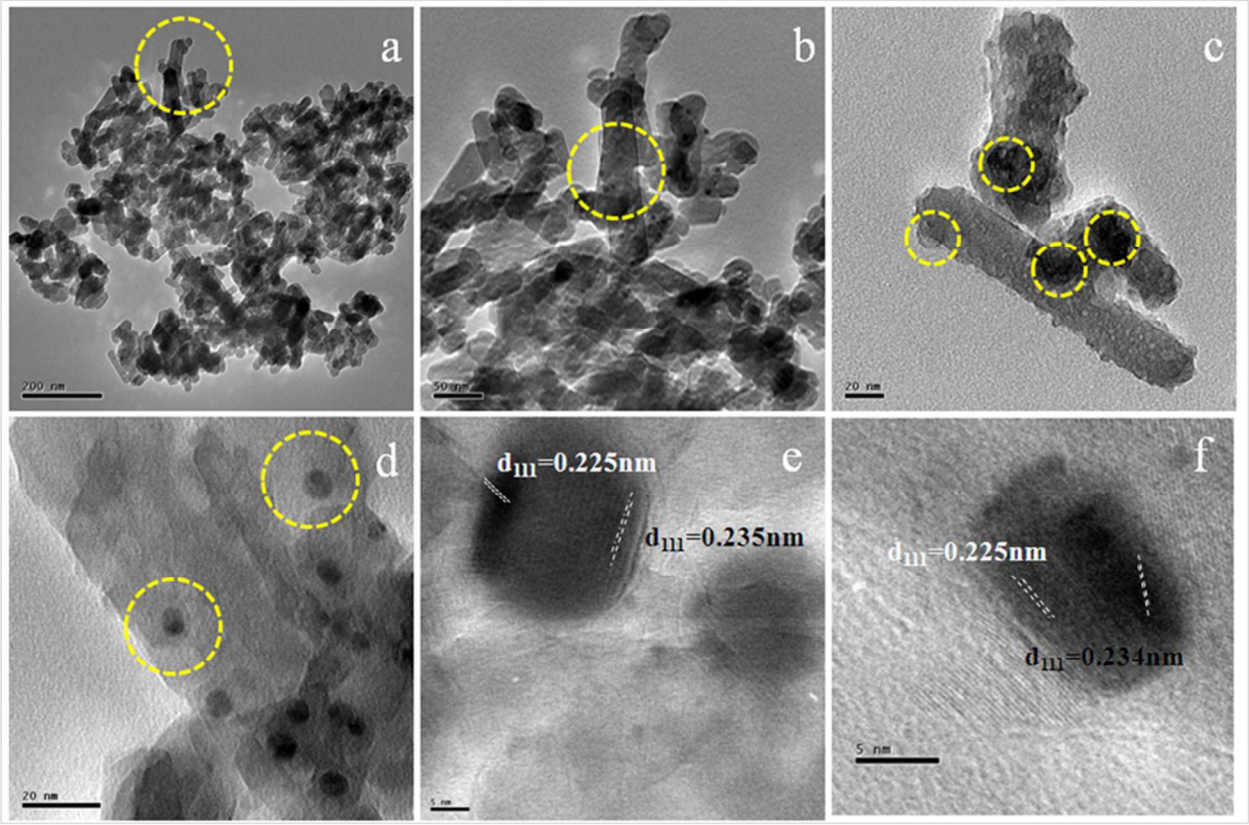


**Fig.15.** HR-TEM images of $Au_{0.8}Pd_{0.2}$/HAP-T (a-e) and $Au_{0.6}Pd_{0.4}$/HAP-T (f) catalysts.

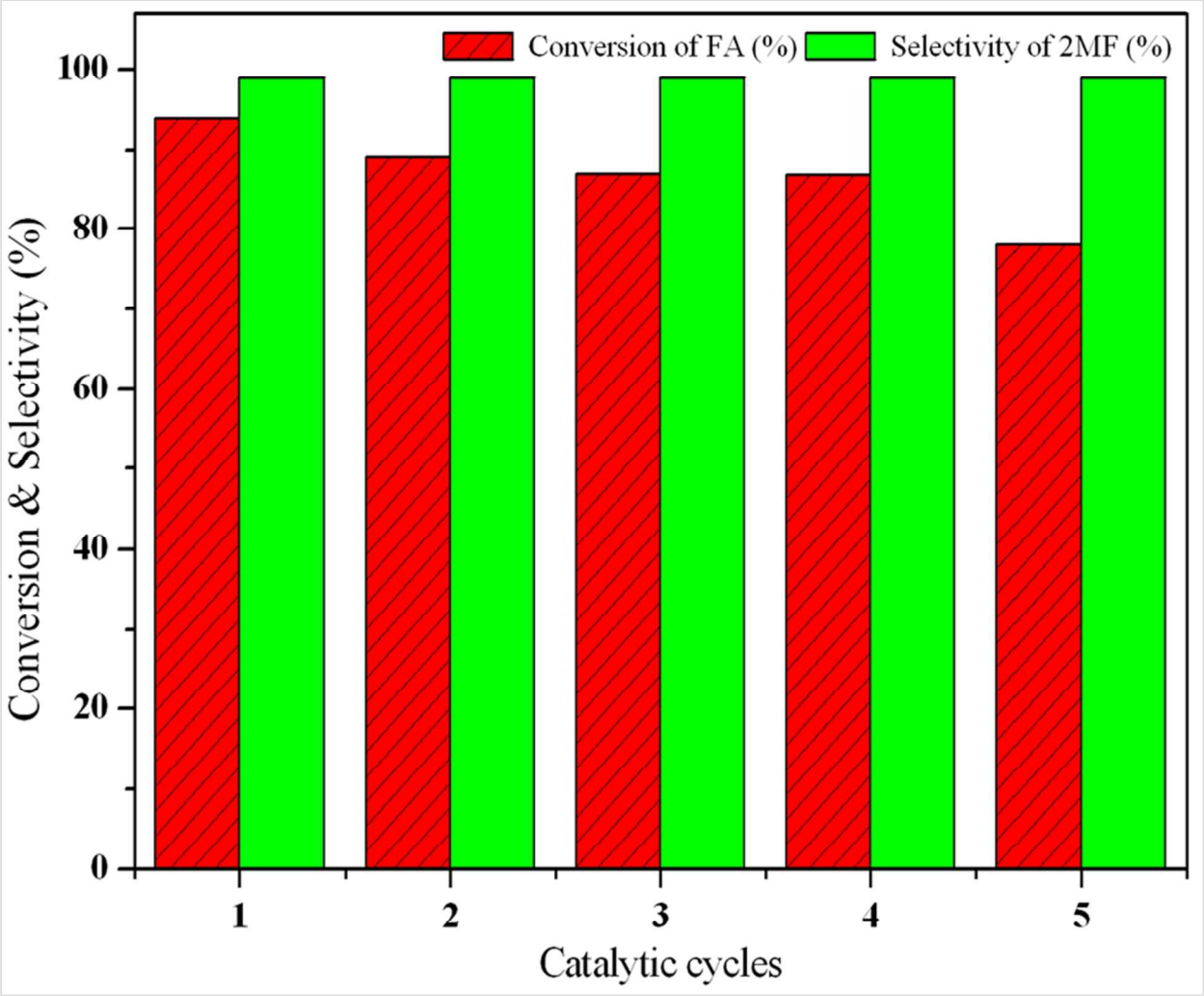


**Fig.16.** Effect of recyclability of $Au_{0.8}Pd_{0.2}$/HAP-T on conversion and selectivity in the oxidative esterification of furfural.

## TABLES

**Table.1** Average particle size of different hydroxyapatite as calculated by XRD and HR-TEM studies.

| Catalysts | Particle size | | Catalysts | Particle size | |
|---|---|---|---|---|---|
| | XRD (nm) | TEM (nm) | | XRD (nm) | TEM (nm) |
| Au/HAP-T | 10.9 | 12.0 | | | |
| $Au_{0.8}Ag_{0.2}$/HAP-T | 17.4 | - | $Au_{0.8}Pd_{0.2}$/HAP-T | 9.7 | 8.5 |
| $Au_{0.6}Ag_{0.4}$/HAP-T | 21.9 | - | $Au_{0.6}$ $Pd_{0.4}$/HAP-T | 9.3 | 9.4 |
| $Au_{0.4}Ag_{0.6}$/HAP-T | 23.5 | - | $Au_{0.4}$ $Pd_{0.6}$/HAP-T | 9.5 | - |
| $Au_{0.2}Ag_{0.8}$/HAP-T | 24.7 | - | $Au_{0.2}$ $Pd_{0.8}$/HAP-T | 9.8 | - |
| Ag/HAP-T | 32.7 | 25.6 | Pd /HAP-T | 13.7 | 20.9 |

**Table.2** d-spacing and lattice parameter values of mono and bimetallic hydroxyapatites.

| Catalysts | d spacing (nm) | | Lattice Parameter (nm) | |
|---|---|---|---|---|
| | Au(111) | Pd(111) | Au(111) | Pd(111) |
| Au/HAP-T | 0.2361 | - | 0.4089 | - |
| $Au_{0.8}Pd_{0.2}$/HAP-T | 0.2352 | 0.2263 | 0.4073 | 0.3923 |
| $Au_{0.6}$ $Pd_{0.4}$/HAP-T | 0.2344 | 0.2265 | 0.4065 | 0.3923 |
| $Au_{0.4}$ $Pd_{0.6}$/HAP-T | 0.2331 | 0.2267 | 0.4032 | 0.3927 |
| $Au_{0.2}$ $Pd_{0.8}$/HAP-T | - | 0.2269 | 0.4029 | 0.3930 |
| Pd/HAP-T | - | 0.2271 | - | 0.3939 |
| JCPDS | 0.2355 | 0.2246 | 0.4079 | 0.3890 |

**Table.3.** Surface metal concentration and binding energy values of mono (Au or Pd) and bimetallic hydroxyapatites (Au & Pd).

| Catalysts Composition | Au (Wt. %) | | Pd (Wt. %) | | Surface conc. of Au:Pd (Wt. %) | Binding Energy(eV) | | | |
|---|---|---|---|---|---|---|---|---|---|
| | Theo | ICP | Theo. | ICP | | Au $4f_{7/2}$ | Au $4f_{5/2}$ | Pd $3d_{3/2}$ | Pd $3d_{5/2}$ |
| Au/HAP-T | 5 | 4.7 | - | - | 2.7:0.0 | 83.37 | 87.03 | - | - |
| $Au_{0.8}$ $Pd_{0.2}$/HAP-T | 4 | 3.6 | 1 | 0.7 | 2.1:0.3 | 83.21 | 86.91 | 335.9 | - |
| $Au_{0.6}$ $Pd_{0.4}$/HAP-T | 3 | 2.8 | 2 | 1.9 | 1.7:1.1 | 82.99 | 86.70 | 336.1 | 341.9 |
| $Au_{0.4}$ $Pd_{0.6}$/HAP-T | 2 | 1.8 | 3 | 2.8 | 0.2:1.9 | - | - | 335.9 | 341.2 |
| $Au_{0.2}$ $Pd_{0.8}$/HAP-T | 1 | 0.8 | 4 | 3.7 | 0.0:2.6 | - | - | 335.6 | 340.8 |
| Pd/HAP-T | - | - | 5 | 4.7 | 0.0:2.8 | - | - | 334.9 | 340.3 |

**Table.4** Surface metal concentration and binding energy values of mono (Au or Ag) and bimetallic hydroxyapatites (Au & Ag).

| Catalysts Composition | Au (Wt. %) | | Ag (Wt. %) | | Surface conc. of Au:Ag (Wt. %) | Binding Energy(eV) | | | |
|---|---|---|---|---|---|---|---|---|---|
| | Theo. | ICP | Theo. | ICP | | Au $4f_{7/2}$ | Au $4f_{5/2}$ | Ag $3d_{5/2}$ | Ag $3d_{1/2}$ |
| Au/HAP-T | 5 | 4.7 | - | - | 2.7 | 83.37 | 87.03 | - | - |
| $Au_{0.8}Ag_{0.2}$/HAP-T | 4 | 3.7 | 1 | 0.9 | 2.1:0.4 | 83.43 | 87.12 | 366.7 | - |
| $Au_{0.6}Ag_{0.4}$/HAP-T | 3 | 2.8 | 2 | 1.8 | 1.9:0.97 | 83.46 | 87.12 | 366.8 | - |
| $Au_{0.4}Ag_{0.6}$/HAP-T | 2 | 1.8 | 3 | 2.7 | 1.1:2.1 | 83.50 | 87.24 | 366.9 | 372.6 |
| $Au_{0.2}Ag_{0.8}$/HAP-T | 1 | 0.8 | 4 | 3.8 | 0.45:2.9 | 83.57 | 87.22 | 367.2 | 372.6 |
| Ag/HAP-T | - | - | 5 | 4.8 | 3.9 | - | - | 367.4 | 373.3 |

**Table.5** Effect of temperature on the conversion of furfural and selectivity towards methyl 2-furoate

| Catalysts | Reaction temperature (Kelvin) | Conversion (%) | Selectivity (%) | |
|---|---|---|---|---|
| | | | Methyl 2-furoate | 2-furaldehyde-dimethyl-acetal |
| Au/HAP-T | 333 | 6.4 | 99.0 | - |
| | 353 | 35.9 | 99.0 | - |
| | 373 | 60.3 | 99.0 | - |
| | 393 | 76.0 | 94.2 | 5.8 |
| | 413 | 82.3 | 85.0 | 15.0 |

*Reaction conditions:*
Furfural- 300µl, TBHP- 3eq., 50mg of $Au_1$/HAP catalyst (5 wt% of Au), 20 ml of $CH_3OH$, Reaction Time – 3 hr.

**Table.6** Oxidative esterification of furfural to methyl 2-furoate over mono (Au or Pd) and bimetallic hydroxyapatites (Au and Pd).

| Catalysts | Conversion (%) | Selectivity (%) | |
|---|---|---|---|
| | | Methyl 2-furoate | 2-furaldehyde-dimethyl-acetal |
| Au/ HAP-T | 76.0 | 94.2 | 5.8 |
| $Au_{0.8}Pd_{0.2}$/ HAP-T | 94.2 | 99.0 | 1.0 |
| $Au_{0.6}Pd_{0.4}$/ HAP-T | 87.6 | 77.2 | 22.7 |
| $Au_{0.4}Pd_{0.6}$/ HAP-T | 84.7 | 67.3 | 32.8 |
| $Au_{0.2}Pd_{0.8}$/ HAP-T | 76.9 | 57.2 | 42.8 |
| Pd/ HAP-T | 86.6 | 2.3 | 97.1 |

*Reaction conditions:*
Furfural- 300µl, TBHP- 3eq., 50mg of catalyst, 20 ml of $CH_3OH$, Reaction temperature-393K, Reaction Time – 3 hr.

**Table.7** Oxidative esterification of furfural to methyl 2-furoate over mono (Au or Ag) and bimetallic hydroxyapatites (Au and Ag).

| Catalysts | Conversion (%) | Selectivity (%) | |
|---|---|---|---|
| | | Methyl 2-furoate | 2-furaldehyde-dimethyl-acetal |
| Au/ HAP-T | 76.0 | 94.2 | 5.8 |
| $Au_{0.8}Ag_{0.2}$/ HAP-T | 89.6 | 99.0 | - |
| $Au_{0.6}Ag_{0.4}$/ HAP-T | 72.0 | 96.9 | 3.5 |
| $Au_{0.4}Ag_{0.6}$/ HAP-T | 71.2 | 85.0 | 14.0 |
| $Au_{0.2}Ag_{0.8}$/ HAP-T | 40.6 | 64.6 | 34.0 |
| Ag/ HAP-T | 72.0 | 25.0 | 75.0 |

*Reaction conditions:*
Furfural- 300µl, TBHP- 3eq., 50mg of catalyst, 20 ml of $CH_3OH$, Reaction temperature-393K, Reaction Time – 3 hr.

**Table.8** Effect of air, oxygen and bases on conversion and selectivity in the oxidative esterification of furfural.

| Catalysts | Base | Conversion (%) | Selectivity (%) | |
|---|---|---|---|---|
| | | | Methyl 2-furoate | 2-furaldehyde-dimethyl-acetal |
| $Au_{0.8}Pd_{0.2}$/ HAP-T + air | - | 0 | 0 | 0 |
| $Au_{0.8}Pd_{0.2}$/ HAP-T + $O_2$ | - | 5.8 | 99.0 | 1.0 |
| $Au_{0.8}Pd_{0.2}$/ HAP-T + $O_2$ | NaOH | 60.4 | 98.0 | 2.0 |
| $Au_{0.8}Pd_{0.2}$/ HAP-T + $O_2$ | $NaOCH_3$ | 78.1 | 96.0 | 4.0 |
| $Au_{0.8}Pd_{0.2}$/ HAP-T + $O_2$ | $K_2CO_3$ | 69.6 | 99.0 | 1.0 |
| $Au_{0.8}Pd_{0.2}$/ HAP-T + $O_2$ + TBHP | - | 94.3 | 99.0 | 1.0 |
| $O_2$ + TBHP | - | 0 | 0 | 0.0 |
| $Au_{0.8}Pd_{0.2}$/ HAP-T+ TBHP | | 94.2 | 99.0 | 1.0 |

*Reaction conditions:*
Furfural- 300µl, 50mg of catalyst, 20 ml of $CH_3OH$, Reaction temperature-393K, Reaction Time – 3 hr, $O_2$ was pressurized using rubber bladder .

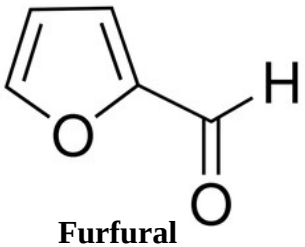


Furfural

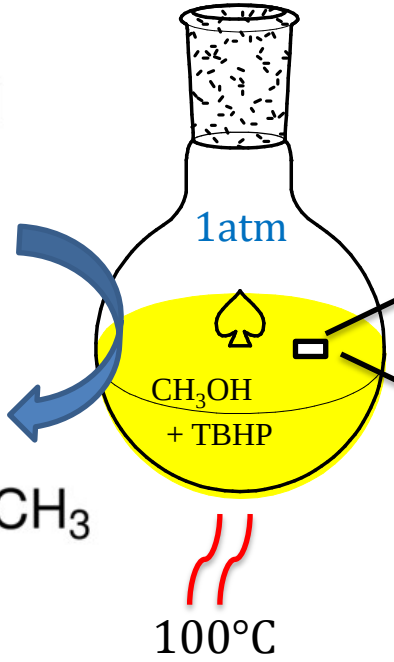


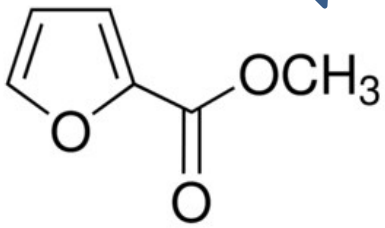


Methyl 2-furoate

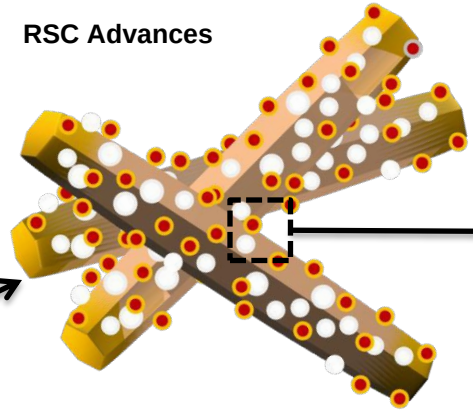

Au/Pd – HAP core shell

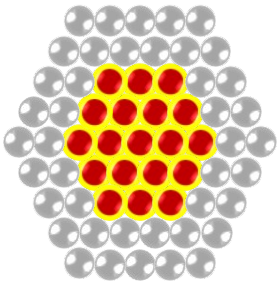

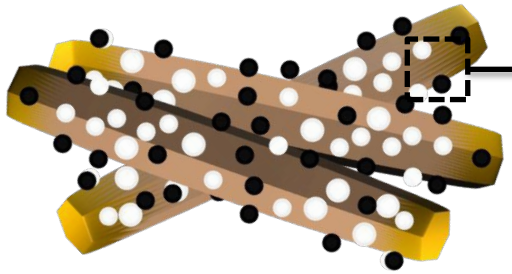

Au/Ag - HAP alloy

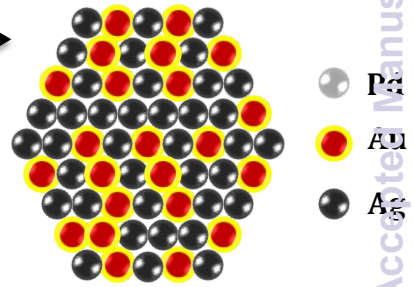


**Bimetallic HAP porous nano rods**